GEORG-AUGUST-UNIVERSITÄT
GÖTTINGEN IN PUBLICA COMMODA SEIT 1737

Fakultät für
Physik

Master's Thesis

Joint Analysis of the $t\bar{t}Z$ and tZq Processes in Trileptonic Final States with ATLAS at $\sqrt{s} = 13\,\text{TeV}$ through Effective Field Theory

Gemeinsame Analyse der $t\bar{t}Z$ und tZq Prozesse in trileptonischen Endzuständen mit ATLAS bei $\sqrt{s} = 13\,\text{TeV}$ mittels effektiver Feldtheorie

prepared by

Daniel Werner

from Wuppertal

at the II. Physikalischen Institut

Thesis number:	II.Physik-UniGö-MSc-2024/06
Thesis period:	1st October 2023 until 30th September 2024
First referee:	Prof. Dr. Arnulf Quadt
Second referee:	apl. Prof. Dr. Jörn Große-Knetter

Abstract

Effective Field Theory is a promising bottom-up approach to searching for Beyond the Standard Model physics. This thesis shows the complete workflow of performing such an analysis on top quark production processes in association with vector bosons. For this analysis, the $t\bar{t}Z$ and tZq production processes were studied in their trileptonic final states. All fits were performed on Asimov data to determine the sensitivity.

The results of this search show large statistical uncertainties for most of the studied Wilson coefficients. The highest sensitivity was reached for $c_{tB}^{(\mathrm{Re})} = 0.00^{+0.84}_{-0.81}$ (stat.)$^{+0.28}_{-0.29}$ (syst.). This result is not as precise as similar analyses but shows the success of the implemented analysis workflow.

In preparation for the High-Luminosity-LHC and its challenges to computing power, new data formats and tools are being developed. These tools are already utilised in this thesis, despite still working in the environment of ATLAS during Run 2. A complete workflow is created, starting from the centralised inputs used for most analyses and leading to EFT results. This approach proves the viability of the new software for future analyses and can serve as an example of its use.

Zusammenfassung

Die Effektive Feldtheorie ist ein vielversprechender Ansatz für die Suche nach Physik jenseits des Standardmodells. Diese Arbeit zeigt den kompletten Arbeitsablauf einer solchen Analyse von Top-Quark-Produktionsprozessen in Verbindung mit Vektorbosonen. Für diese Analyse wurden die Produktionsprozesse von $t\bar{t}Z$ und tZq in ihren trileptonischen Endzuständen untersucht. In allen Messungen wurden Asimov-Daten verwendet, um die Empfindlichkeit der Analyse zu bestimmen.

Die Ergebnisse zeigen große statistische Unsicherheiten für die untersuchten Wilson-Koeffizienten. Die höchste Empfindlichkeit wurde mit $c_{tB}^{(\mathrm{Re})} = 0.00^{+0.84}_{-0.81}$ (stat.)$^{+0.28}_{-0.29}$ (syst.) erreicht. Dieses Ergebnis ist zwar weniger präzise als ähnliche Analysen, zeigt aber den Erfolg des implementierten Analyse-Workflows.

In Vorbereitung auf den High-Luminosity-LHC und die damit verbundenen Herausforderungen an die Rechenleistung werden derzeit neue Datenformate und Tools entwickelt. Die neue Software wird in dieser Analyse bereits verwendet, obwohl die simulierten Daten auf dem ATLAS Detektor während des LHC Run 2 beruhen. Es wird ein vollständiger Workflow erstellt, beginnend bei den Rohdaten im standardisierten Format, bis hin zu den EFT-Ergebnissen. Dieser Ansatz beweist die Einsatzfähigkeit der neuen Software für zukünftige Analysen und kann als Beispiel für ihre Verwendung dienen.

Contents

1. Introduction

The last century of studying particle physics in nature and accelerators has led to the development of the Standard Model of particle physics. While particle accelerators started at the comparatively low energy of 50 keV in 1928 [1], they are nowadays capable of reaching 6.8 TeV of energy per particle. With the Standard Model as a precise and successful theory, recent work is largely focused on studying the phenomena unexplained by the Standard Model. The alternative theories developed to explain these effects are usually referred to as *Beyond the Standard Model* theories.

Besides increasing the available energy at colliders, a large number of events is needed to have sufficient statistical power for discoveries. The High-Luminosity-LHC is the next big step on the path towards many events by increasing the luminosity of colliders. This upgrade will take place in the years 2026 to 2029 and will see upgrades in many key components of the accelerator to increase the luminosity delivered to the experiments [2]. In the 11 years of operation following the upgrade, an integrated luminosity of around $3\,\mathrm{ab}^{-1}$ will be delivered, which is more than six times as much luminosity as delivered in the 14 years leading up to the upgrade. The High-Luminosity-LHC will bring challenges to the data analysis as well. By increasing the luminosity, the number of recorded events will rise too. This increase requires new software tools to analyse the data and new solutions for storing it. To ensure a smooth start of analyses with these large datasets, it is important to develop already and test the tools in preparation for the upgrade.

While there are different methods in searching for Beyond the Standard Model physics effects, Effective Field Theory is of special interest. In this approach, new phenomena can be described and discovered without needing a complete alternative model. While many analyses include interpretations of their results regarding Effective Field Theories, dedicated large searches are rare. In a global fit for Effective Field Theory effects, many parameters and processes could be covered simultaneously. First efforts towards such a global search in processes containing a top quark have been made by CMS recently [3] and it is upon ATLAS to follow up on this with a similar search.

Performing the fits needed for such a global search is a very time- and resource-consuming process. Therefore, it provides an excellent opportunity to apply the new tools developed for analyses in the High-Luminosity-LHC environment. While adapting early to new software has the risk of encountering bugs, it is important for the collaboration as a whole to find and fix such bugs. The advantages of using the new software are the ability to profit off the improved performance and the chance to influence the development towards helpful features for analyses. This analysis aims to create a workflow to perform searches for Effective Field Theory effects with new software tools and to study the usability and performance of the tools. In addition, the search for new effects will be performed as broadly as possible to move towards a global search in the near future.

2. The Standard Model of Particle Physics

The Standard Model (SM) of particle physics is a description of the elementary particles and the fundamental forces that govern the interactions between the particles [4]. For each force, additional force-carrying particles are included in the SM. While being a precise theory to describe the physics currently observed, some phenomena are not covered by the SM. These include the nature of dark matter hinted at in astrophysics [5] and the asymmetry of matter and antimatter in our observable universe [6].

2.1. Elementary Particles

The SM consists of quarks, leptons and bosons as seen in Figure 2.1. Both quarks and leptons are spin-$^1\!/_2$ fermions and make up all matter. Quarks are organised into three generations that each contain an up-type quark with electric charge $+^2\!/_3\,e$ (up, charm, top) and a down-type quark with a charge of $-^1\!/_3\,e$ (down, strange, bottom).

Similarly, the leptons are split into the charged down-type leptons with charge $-e$ (electron, muon, tau) and the neutral up-type neutrinos. These neutrinos are named electron-neutrino, muon-neutrino, and tau-neutrino corresponding to the electrically charged partner in each generation. The charge distinguishing between up- and down-type particles is the third component I_3 of the weak isospin I. Fermions can occur with a left-handed or right-handed chirality. Left-handed particles form doublets with $I_3 = \pm^1\!/_2$ while right-handed particles form singlet states with $I_3 = 0$. The $I_3 = +^1\!/_2$ entries correspond to the up-type particles with $I_3 = -^1\!/_2$ signifying down-type particles.

Unlike leptons, the quarks carry a colour charge that can take the values red, green, or blue. In composite particles, the total colour charge must be neutral. The analogy of colour is chosen for this charge since the combination of all three values leads to a neutral *white* state. A neutral state can also be achieved by combining a colour with its corresponding anti-colour. The bound states formed by quarks are sorted into groups according to their quark numbers and total spin. The most commonly found bound states

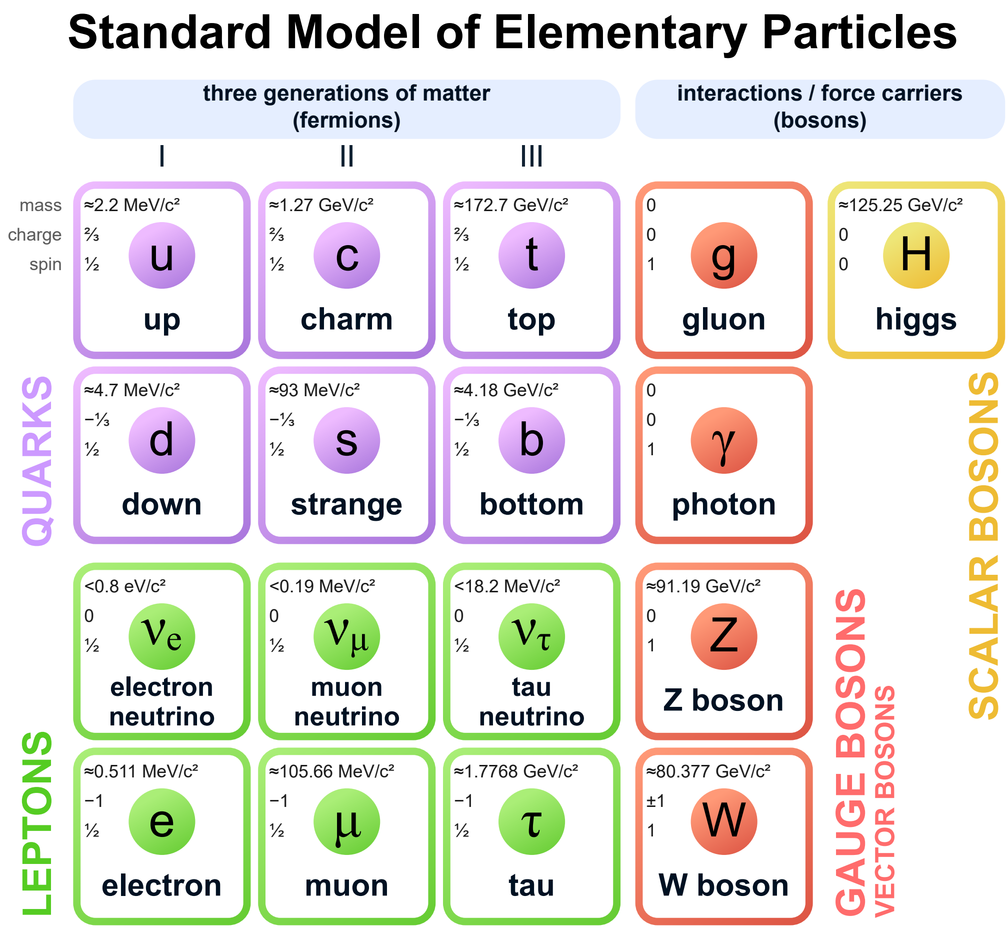

Figure 2.1.: The Standard Model of Particle Physics sorts all known elementary particles into quarks, leptons, and bosons. For each particle the mass, charge and spin are included based on [11]. [Modified graphic, Original by Cush, Public domain, via Wikimedia Commons]

are mesons made of two quarks with an integer spin and half-integer baryons made up of three quarks. In addition, exotic hadrons like tetraquarks or pentaquarks made up of four and five quarks are allowed in the SM. Both types of hadrons have been observed by the LHCb experiment [7–10].

The SM also contains antiparticles for all the fermions. An antiparticle generally has the same mass and lifetime as its particle counterpart. Any charges that can take opposite values will do so for antiparticles. For the electric charge and the third component of the weak isospin, this corresponds to negative values, while the colour charge of antiquarks can be anti-red, anti-green, or anti-blue.

Besides the fermions, the SM also contains integer-spin bosons. The spin-1 vector gauge bosons are associated to the fundamental forces explained in Section 2.2 as mediator particles. Photons (γ) and gluons (g) as the mediator particles of the electromagnetic and strong force, respectively, are massless particles. In contrast, the $W^{\pm}$ and Z bosons mediating the weak interaction are massive. The current world average masses for both particles are $m_W = 80.377 \pm 0.012\,\mathrm{GeV}$ [11] and $m_Z = 91.1876 \pm 0.0021\,\mathrm{GeV}$ [11]. There is a single scalar spin-0 Higgs boson (H) as the excited state of the Higgs field. The Higgs boson has a mass measured as $m_H = 125.25 \pm 0.17\,\mathrm{GeV}$ [11] in the world average.

2.2. Interactions

The particles in the SM interact with each other via the three fundamental forces. Each of these forces couples to a specific charge. Mathematically, the interactions can be described through symmetry groups that give rise to the mediating bosons listed in Section 2.1. Gravity, which is considered a fourth fundamental force in the universe, is not included in the SM.

In the 1960s, the electromagnetic and the weak interactions were unified and described as one interaction by Glashow, Salam, and Weinberg [12–14]. This theory is based on a $SU(2)_I \times U(1)_Y$ symmetry in weak isospin I and weak hypercharge Y. From this symmetry, the four fields $W^1_\mu, W^2_\mu, W^3_\mu$, and B_μ arise. The Brout-Englert-Higgs-Guralnik-Kibble-Hagen mechanism[1] [15–18] introduces a field to the SM with a degenerate minimum energy state that leads to spontaneous symmetry breaking. The electroweak (EW) fields can be rearranged into superpositions that couple differently to the Higgs field. These obtained fields are identified with the physically observed bosons γ, W, and Z. The coupling of the W and Z bosons to the Higgs field leads to these bosons being massive, while the photon remains massless. The masses of the W and Z bosons make these bosons unstable and thus limit the range of the weak interaction. Since the photon is massless and neutral, the electromagnetic force has an unlimited range as observed in macroscopic situations.

In weak processes, the coupling strength is determined by a superposition of the weak isospin and the electric charge. For charged currents mediated by W bosons, the coupling strength becomes 0 for right-handed particles. Therefore, the W boson only couples to the left-handed doublets and can change the particles into each other. In contrast to the W boson, the Z boson mediates weak neutral currents and couples to both up- and down-type particles. Charged currents involving quarks can contain flavour changes with vertex factors modified by the Cabibbo-Kobayashi-Maskawa-Matrix (CKM-Matrix, V_{CKM}) [19].

The underlying symmetry of the strong interaction is a $SU(3)_\mathrm{C}$ symmetry in colour charge [20, 21]. From the Gell-Mann matrices as generators, eight massless bosons arise that are

---

[1] short Higgs mechanism

called gluons. While the gluons are massless, they are not neutral in terms of their colour charge. This allows a self-interaction between gluons, which limits the range of the strong interaction. When quarks with high momenta interact via the strong interaction, the energy density of the gluon field can grow sufficiently large to allow for pair-production of additional quarks. These quarks form hadrons and move along the original quarks in sprays of particles that are called jets. Due to its coupling to the colour charge, the strong force is also referred to as quantum chromodynamics (QCD).

The Higgs field couples not only to bosons but to fermions as well. Through the interaction between fermions and the Higgs field, the masses of the fermions can be expressed in a gauge invariant way in the mathematical description of the SM. The mass of a fermion is then proportional to the Higgs-Yukawa coupling between the particle and the Higgs field. In consequence, the Higgs field couples to all massive particles in the SM.

2.3. The Top Quark

The top quark was discovered in the CDF and DØ experiments at the Tevatron with masses of 176 ± 8 (stat.) $\pm\ 10$ (syst.) GeV [22] and 199^{+19}_{-21} (stat.) $\pm\ 22$ (syst.) GeV [23] making it the heaviest known particle in the SM. Since then, further measurements at both the Tevatron and the Lhc have contributed to a current world average mass of $m_t = 172.69 \pm 0.30\,\text{GeV}$ [11]. By being heavier than the W, the decay of the bare top quark can happen through an on-shell W boson and does not suffer from any kinematic suppression. Its resulting width of $\Gamma_t = 1.42^{+0.19}_{-0.15}\,\text{GeV}$ [11] allows the calculation of the decay time $\tau_t = \Gamma_t^{-1}$. The decay time of $\tau_t \approx 5 \times 10^{-25}\,\text{s}$ is smaller than the timescales at which hadronisation occurs. Consequently, the top quark is the only quark that does not form bound states but decays as a bare quark.

Top quark production modes

The available initial state particles at the Lhc are the valence quarks (u and d), the sea quarks, and gluons. Parton distribution functions (PDFs) can be used to compute the probability of finding any parton as part of a proton carrying a momentum fraction x. Starting with these initial state particles, pairs of top and antitop quarks can be produced via the strong interaction. The Feynman diagrams of this process at lowest order are shown in Figure 2.2. Single top quarks can only be produced through the weak interaction. In this process, a down-type antiquark needs to be involved due to charge and weak isospin conservation. This quark is almost exclusively a bottom quark as the CKM-matrix suppresses other combinations through $|V_{tb}| \gg |V_{ts}|, |V_{td}|$ [19]. The

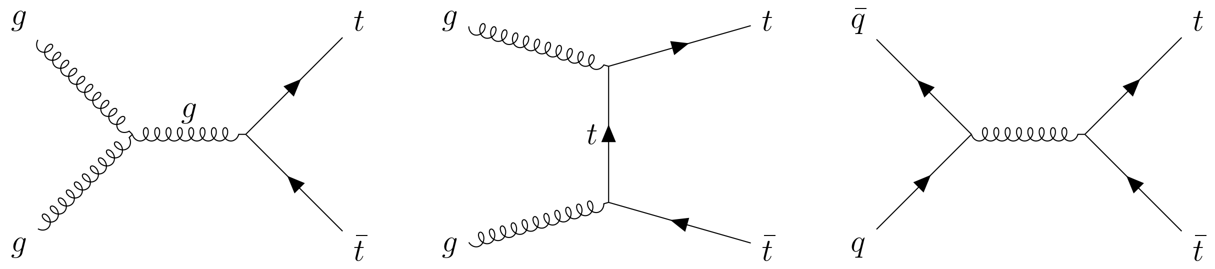

Figure 2.2.: Production of a $t\bar{t}$ pair via gluon-gluon fusion (left), the t-channel (middle), and quark-antiquark annihilation (right).

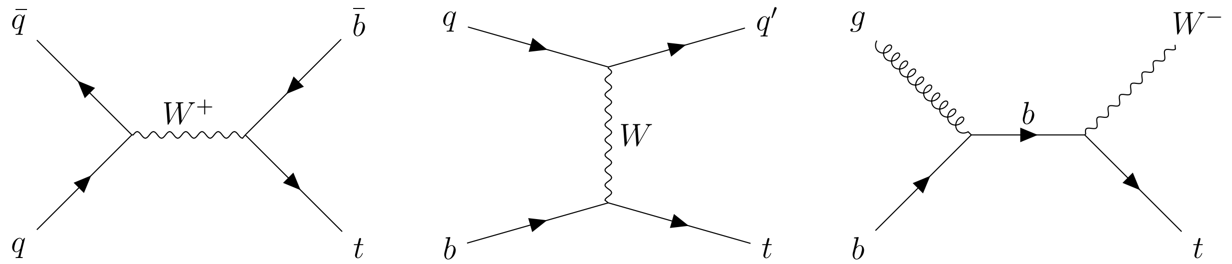

Figure 2.3.: Production of a single top quark via the s-channel (left), the t-channel (middle), and in association with a W boson (right).

production diagrams for single top quarks as seen in Figure 2.3 are an s-channel and t-channel diagram and the associated production of a top quark with a W boson. In the processes containing a bottom quark in the initial state, these quarks can either occur as sea quarks in the colliding protons or they are created by a gluon splitting into a $b\bar{b}$ pair. Including bottom quarks as a fifth flavour of sea quarks is called the five flavour scheme (5FS), while the alternative approach is the four flavour scheme (4FS).

In the search for *Beyond the Standard Model* (BSM) physics, the couplings of the Z boson to the top quark is of great interest as further explained in Section 2.4. To study this coupling, the production of top quarks in association with the Z boson can be studied, resulting in $t\bar{t}Z$, tZq, and tWZ production. $t\bar{t}Z$ is produced through the radiation of an additional Z boson in the $t\bar{t}$ production. When the Z boson is radiated from the top quark, the cross-section of the process is influenced by modifications to the tZ coupling. Initial state radiation in the quark-antiquark annihilation adds a process that does not contain this coupling but interferes with the other diagrams. The inclusive $t\bar{t}Z$ cross-section has been predicted at next-to-leading-order (NLO) and next-to-next-to-leading

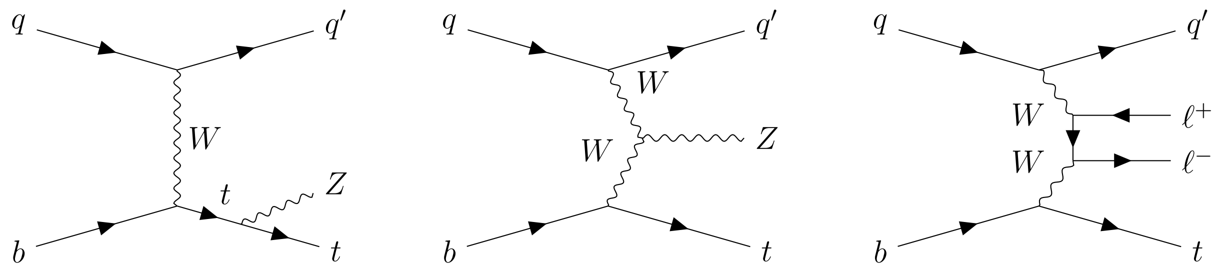

Figure 2.4.: tZq production can occur through multiple modifications of single top production. Notable processes include the Z radiation from the top quark (left), the WWZ vertex (middle) and the non-resonant contribution (right).

logarithmic (NNLL) accuracy to be [24]

$$\sigma_{t\bar{t}Z} = 863^{+73}_{-85}\ (\text{scale variations}) \pm 28\ (\alpha_\text{s} \oplus \text{PDF})\,\text{fb}\ .$$

The most recent measurements at Atlas found the cross-section of these processes to be $\sigma_{t\bar{t}Z} = 860 \pm 40$ (stat.) ± 40 (syst.) fb [25] in agreement with the prediction. Cms measured the cross-section as 950 ± 50 (stat.) ± 60 (syst.) fb [26] which is compatible with both the SM prediction and the Atlas result.

The first two production modes of single top quarks can be modified to produce the tZq final state if any of the particles radiate a Z boson. Besides the top-Z coupling and the coupling of the Z to other quarks, the W-Z coupling influences this process as the W boson can also radiate the Z boson. Examples of these processes can be seen in Figure 2.4. Typically studied final states of tZq involve the Z decaying into a pair of charged leptons $\ell^+\ell^-$. This final state includes a non-resonant contribution from W bosons as seen in the right diagram of Figure 2.4. The most recent cross-section measurements for this process found $\sigma_{tZq} = 97 \pm 13$ (stat.) ± 7 (syst.) fb at Atlas [27] and $\sigma_{tZq} = 87.9^{+7.5}_{-7.3}$ (stat.)$^{+7.3}_{-6.0}$ (syst.) fb at Cms [28]. From these measurements, it is visible that tZq production is rare compared to $t\bar{t}Z$. In the production of a single top quark in association with a W, a Z can be radiated to create the tWZ final state. When considering higher-order diagrams contributing to this final state, tWZ can occur as a $t\bar{t}Z$ final state where one top quark has decayed. As a consequence, the tWZ process interferes with the $t\bar{t}Z$ process at NLO [29] making them important processes to study simultaneously. The cross-section of tWZ production was first measured by Cms as $\sigma_{tWZ} = 354 \pm 54$ (stat.) ± 95 (syst.) fb [30].

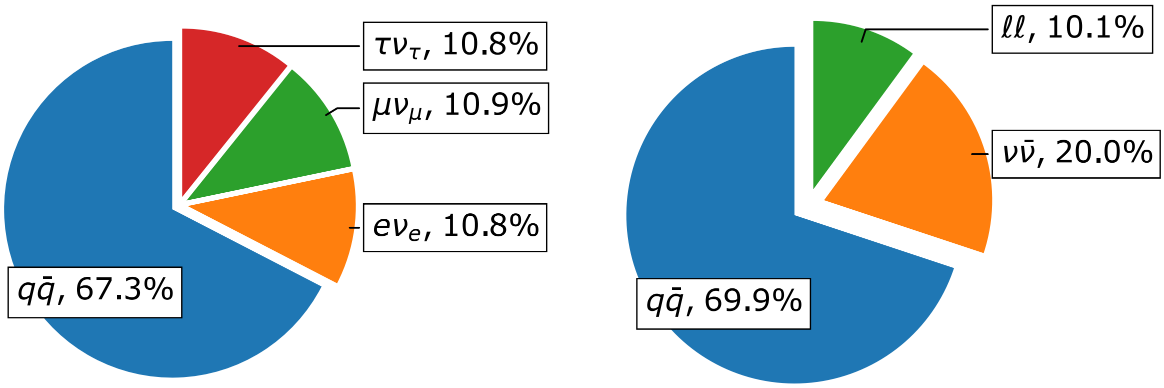

(a) W boson (b) Z boson

Figure 2.5.: Branching ratios for the decay of (diagram a) a W boson according to [31] and (diagram b) a Z boson according to [32].

Top quark decay modes

The top quark decays almost exclusively into a bottom quark with the current world average of the branching found to be [11]:

$$\mathcal{R} = \frac{\mathcal{B}(t \to Wb)}{\mathcal{B}(t \to Wq)} = 0.957 \pm 0.034 \ .$$

In consequence, the final state of any process will contain one b per top quark involved. The additional W^+ decays into a charged lepton (e^+, μ^+, τ^+) with its corresponding neutrino (ν_e, ν_μ, ν_τ) or a quark-antiquark pair according to its branching ratios [31] shown in Figure 2.5. The electron and muon live long enough to be detected in the detector directly, while tau decays within the beam pipe leading to its decay products being detected. When referring to leptonic final states, only decays to electrons and muons are considered here. Any quarks form jets in the detector, which are called b-jets if they originate from a bottom quark. The neutrinos created together with the charged leptons hardly interact with matter and are generally not reconstructed by the detector. In processes involving two tops, either one can decay leptonically into $b\ell\nu_\ell$ with $\ell = (e, \mu)$ or hadronically into any other final state. The possible combinations for the two top quarks are then the dileptonic, the semileptonic, the fully hadronic, and the $\tau +$ jets channel. Z bosons can decay into quark pairs $q\bar{q}$, opposite-sign-same-flavour (OSSF) lepton pairs $\ell^+\ell^-$, and neutrino pairs $\nu\bar{\nu}$ that are invisible in the final state. The branching ratios for the Z are visualised in Figure 2.5.

In the associated production processes of top quarks and Z bosons, the decay channels of the top quarks are combined with those of the Z and possibly W bosons.

2.4. Standard Model Effective Field Theory

The SM can be described through its Lagrangian $\mathcal{L}$ that contains all fields of the SM and their interactions. As explained in Section 2.2, the entire Lagrangian has to obey the symmetries $U(1)_Y \times SU(2)_I \times SU(3)_\mathrm{C}$. The operators in the SM Lagrangian are of mass dimension four. The basic assumption of Standard Model Effective Field Theory (SMEFT) is that the SM is only a low-energy approximation of an underlying theory. This theory would then include some operators of higher order than four in the Lagrangian. In the Lagrangian, the additional operators can be scaled through an energy scale Λ at which the new effects arise. The resulting SMEFT Lagrangian, including dimension five and six operators, can be calculated from the SM Lagrangian as:

$$\mathcal{L}_\mathrm{SMEFT} = \mathcal{L}_\mathrm{SM} + \sum_i \frac{c_i^5 \mathcal{O}_i^5}{\Lambda} + \sum_i \frac{c_i^6 \mathcal{O}_i^6}{\Lambda^2}$$

The operators $\mathcal{O}_i^d$ of dimension d are scaled by Λ^{4-d} and their respective Wilson coefficient c_i^d. These Wilson coefficients are dimensionless and can be interpreted as strength parameters of the interactions described by the operators.

In general, operators of arbitrary dimensions can be considered. As operators are more strongly suppressed, the higher their dimension is, searches for SMEFT effects usually focus on the lowest available dimensions. Any operator of an odd dimension must violate the conservation of lepton and baryon number [33, 34]. By requiring these conservation laws to be fulfilled, the lowest dimension operators for SMEFT are of dimension six. The 34 remaining operators of dimension six according to [35] are shown in Figure 2.6.

The overlapping rectangles in the diagram show which processes are affected by each Wilson coefficient and can be used to study the coefficients. In this analysis, $t\bar{t}Z$ production is studied as an association $t\bar{t}$ production with a vector boson, and tZq is an example of electroweak single-top production. The overlap between these categories contains the four coefficients c_{Ht}, c_{tB}, c_{tW}, and $c_{Qq}^{3,1}$. The first of these modifies the interaction between the Higgs boson and right-handed top quarks. In the notation of the commonly used Warsaw basis [36], this operator corresponds to $c_{\varphi u}^{(33)}$ with (33) corresponding to the flavour indices of the involved top quarks and the Higgs doublet φ. The interactions of top quarks with the electroweak fields are modified through c_{tB} and c_{tW}. As introduced in Section 2.2, these fields can be rearranged into the fields corresponding to physical bosons. Through the same superposition, the Wilson coefficient affecting the interaction with the Z boson

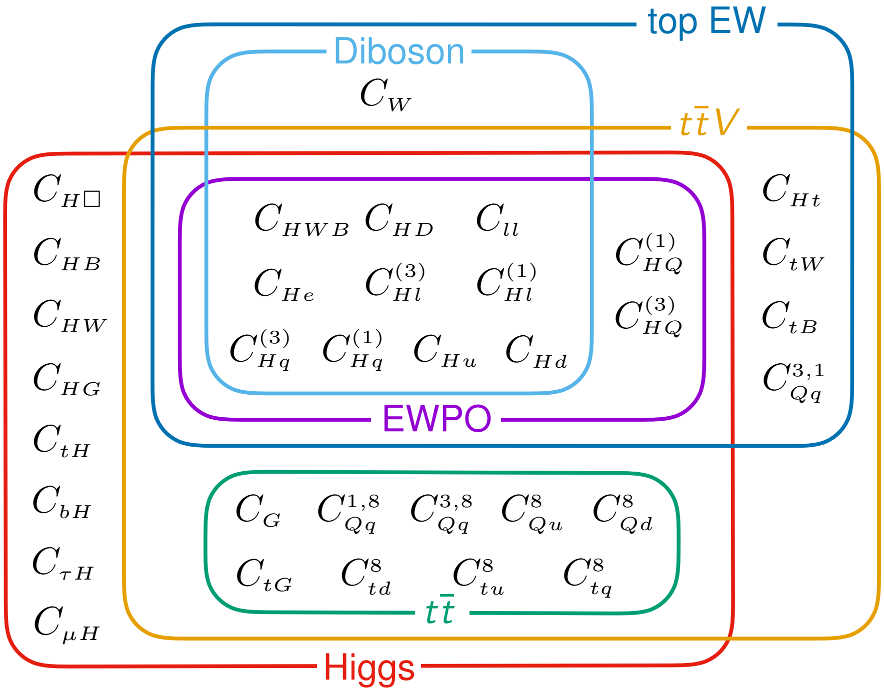

Figure 2.6.: Wilson coefficients associated with SMEFT operators of dimension six sorted by the processes they affect [35].

is obtained:

$$c_{tZ} = \mathrm{Re}\left\{-\sin(\theta_W)c_{tB} + \cos(\theta_W)c_{tW}\right\} \ . \tag{2.1}$$

As a consequence, the real parts $c_{tB}^{(\mathrm{Re})}$ and $c_{tW}^{(\mathrm{Re})}$ are of special interest in processes contain top quarks and Z bosons. The last of the four coefficients, $c_{Qq}^{3,1}$, corresponds to a BSM vertex of two heavy flavour quarks (Q) and two light flavour quarks (q). This vertex modifies the cross-section for $t\bar{t}$ production instead of the interaction between the top and Z bosons and is not considered for this analysis. Two additional coefficients that are also affected by electroweak precision measurements and the Higgs boson are $c_{HQ}^{(1)}$ and $c_{HQ}^{(3)}$. These coefficients are relevant in interactions between a Higgs boson and quarks in the left-handed heavy flavour doublet. A calculation of the top-Z interaction vertex shows that c_{Ht}, $c_{HQ}^{(1)}$ and$c_{HQ}^{(3)}$ modify the vector and axial parts of the Z interaction [37]. Another result of the calculation is that $c_{tB}^{(\mathrm{Re})}$ and $c_{tW}^{(\mathrm{Re})}$ lead to electroweak dipole moments that do not occur in the SM since they are suppressed. The first modification leads to a large interference with the SM while the dipole contributions are purely BSM effects and scale proportionally to the four-momentum of the Z boson in the vertex.

SMEFT is a bottom-up approach to searching for BSM physics since it does not require a rigorously defined alternative to the SM. Instead, couplings that show unexpected behaviour can be identified through their Wilson coefficients. The development of new theories to explain the deviations can be done separately after an SMEFT search. In general, the deviations from SMEFT are small at currently available energies due to the suppression scale. Searches rely, in turn, on very precise measurements of the involved processes.

3. The Experimental Setup

3.1. The Large Hadron Collider

The LHC [38] is the largest accelerator in the CERN accelerator complex. Using linear accelerators, the proton synchrotron (PS), and the super proton synchrotron (SPS) as pre-accelerators, the LHC is able to accelerate proton bunches to a maximum energy of 6.8 TeV. The acceleration is achieved via high-frequency cavities. A total of about 1200 superconducting dipole magnets with a strength of 8 T are used to achieve the bending of the beams [38]. The resulting collisions have a center-of-mass energy, $\sqrt{s}$, of 13.6 TeV in Run 3. In the data-taking period of Run 2 in the years 2015 to 2018, the reached energy was $\sqrt{s} = 13\,\text{TeV}$ which is the relevant value for this analysis. The accelerated bunches consist of about 1×10^{11} protons [38] and bunch crossings occur every 25 ns. In each of these bunch crossings, the number of collisions is called μ. When one of these collisions contains a signal event to be studied further, the other collisions are called in-time pileup. Out-of-time pileup occurs when remnants of previous collisions still create a signal in the detector. All types of pileup must be rejected to allow for an accurate reconstruction of the signal. The average value of μ has increased over the past runs of the LHC as can be seen in Figure 3.1. In the years 2026 to 2029, an upgrade called the High-Luminosity-LHC (HL-LHC) for the LHC is planned to increase the luminosity delivered to the experiments [2]. This upgrade will increase the amount of recorded data. In turn, the efficiency of triggering at the detectors and analysing the data will need to be increased to keep up with the growing datasets.

In four of the eight possible interaction points of the LHC, underground halls house the detectors ATLAS [39], ALICE [40], CMS [41], and LHCb [42]. The detectors focus on different parts of the SM with ATLAS and CMS being multi-purpose detectors, while ALICE is specialised on quark-gluon plasma and LHCb studies processes that violate charge-parity symmetry. As this analysis is performed with the ATLAS detector, it will be described in more detail in the following section.

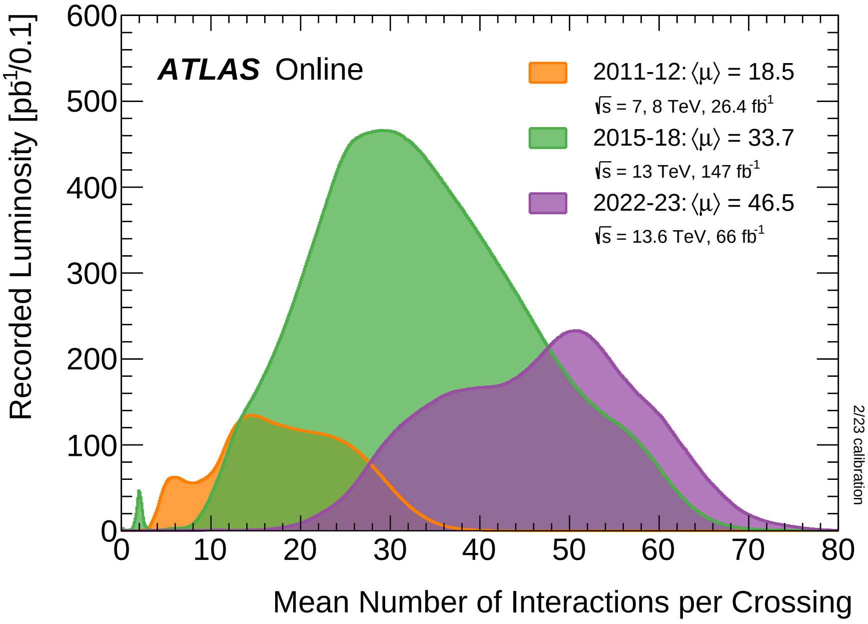

Figure 3.1.: Number of collisions μ at the ATLAS detector recorded in the different runs of the LHC.

3.2. The ATLAS Detector

The ATLAS detector consists of multiple sub-detectors combined in a cylindrical geometry as seen in Figure 3.2. Along the central axis of the cylinder, the beam pipe passes through the detector with collisions occurring near the centre. Around the beam pipe, the Inner Detector (ID) is found, consisting of semiconductor pixel and strip detectors and a transition radiation tracker [39]. These components are designed to detect passing charged particles through ionisation. The resulting measurement is a set of hits that can be combined into the tracks of different particles. The highest precision for position measurements is reached by the pixel detector at 10 µm ($R-\phi$ axes) and 115 µm (z axis) [39]. The ID is surrounded by a superconducting solenoid magnet that creates a longitudinal 2 T magnetic field [39]. This results in helical paths of charged particles moving radially outwards. From this curvature, the momentum of a particle can be measured by the ID. Outside the solenoid, an electromagnetic calorimeter (ECAL) is placed. The calorimeter is made from active liquid Argon (LAr) layers alternating with Lead absorber plates [39]. Through Bremsstrahlung and pair-production in the absorbers, electrons and photons produce particle showers, distributing their energy. These showers continue until the kinetic energy of the involved particles falls below a critical energy, stopping the initial particle effectively. A measurement of the shower size yields information about the particle's energy.

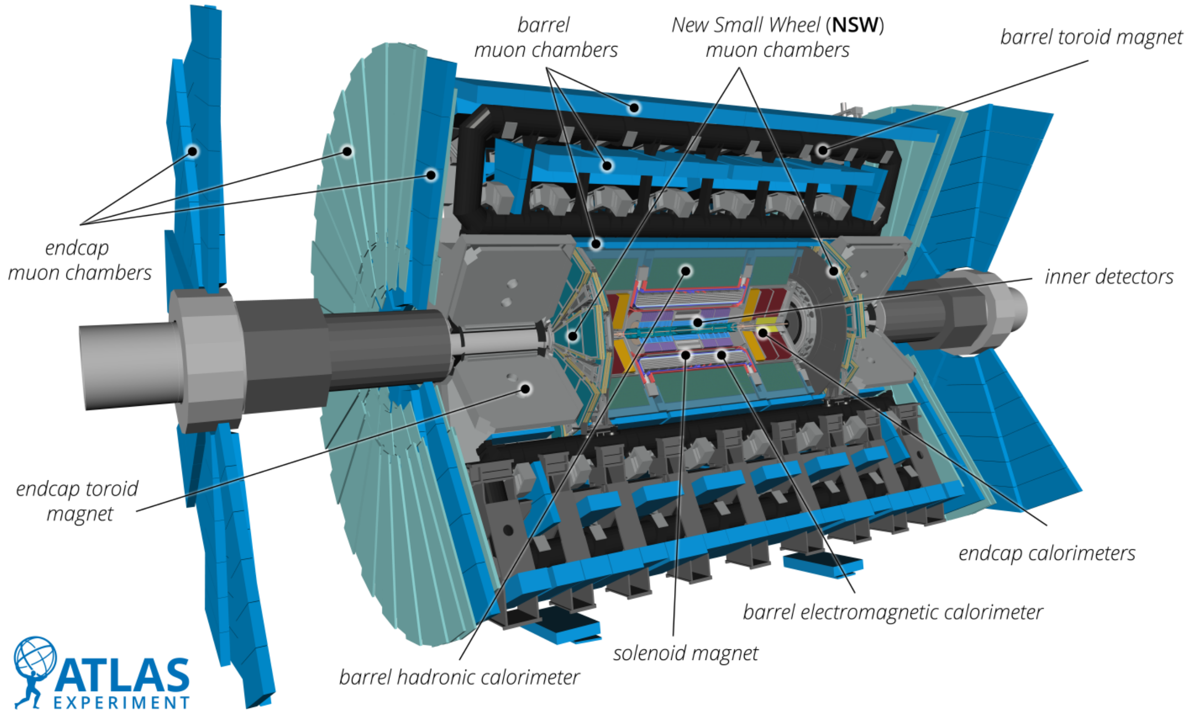

Figure 3.2.: Labelled overview of the ATLAS detector and its components.
ATLAS Experiment © 2008 CERN

To fully stop the particles, the thickness of the calorimeter must be sufficient. The hadronic interaction length is larger than the radiation for electrons and photons in matter. As a consequence, these particles are usually not stopped within the ECAL. To account for this effect, a hadronic calorimeter (HCAL) is placed as the next layer with a higher stopping power due to materials with high atomic numbers. The HCAL in the ATLAS detector consists of active scintillating tiles and steel absorber plates [39]. The hadrons can interact with the iron nuclei through QCD, creating hadronic showers. In the same way as the ECAL, the HCAL measures particle energies.

These components comprise the barrel region of the detector. In the forward and backward regions along the z-axis, the end caps of the detector are located. These contain an ECAL and an HCAL in order to increase the geometry covered by the detector. Both the ECAL and the HCAL in the end caps are made of LAr in combination with lead (ECAL) and copper plates (HCAL) [39]. The forward calorimeter is a LAr calorimeter with copper and tungsten absorbers to measure electromagnetic and hadronic signals very close to the beam pipe [39].

The outermost layers of the detector are gas-filled ionisation detectors meant to measure muons. The detector types in use are monitored drift tubes (MDTs) and cathode strip chambers (CTCs) for tracking, and resistive plate chambers and thing gap chambers for triggering [39]. This Muon System (MS) relies on the fact that muons at the typical energies found at ATLAS are minimum ionising particles that are not stopped by the calorimeters. As a result, any track detected in the MS can be assumed to correspond to a muon.

The ATLAS detector contains a toroidal magnet system located between the layers of the MS and in the end caps that creates a toroidal magnetic field of 0.5 T in the central and 1 T in the end cap MS [39]. This leads to the tracks of muons being curved in the longitudinal direction in order to allow for a better momentum resolution in muons. In the longitudinal direction of the detector, the MS consists of circular wheels. The small wheel is placed between the endcap calorimeter and the endcap of the toroid magnet and was the first component of ATLAS to be added in preparation for the HL-LHC [43, 44]. The other two wheels are placed outside these endcaps as the farthest components from the interaction point.

The detector's cylindrical geometry can be described using a z-axis along the beam pipe and coordinates r and ϕ parametrising the transverse plane. To describe the direction of particles, the longitudinal information is expressed through the pseudorapidity η of the particles. The transverse movement is described using the transverse momentum p_{T} and the azimuthal angle ϕ. Distances between particles can be calculated from the difference in both η and ϕ as $\Delta R = \sqrt{(\Delta\eta)^2 + (\Delta\phi)^2}$. The ID detects particles in a range of $|\eta| < 2.5$ [39]. The calorimeters in the barrel and end cap have a combined coverage of $|\eta| < 3.2$ [39]. The forward calorimeters extend this range to $|\eta| < 4.9$ for both electromagnetic and hadronic measurements. In the MS, the bending of tracks due to the magnetic field is only provided in a range of $|\eta| < 2.7$. Outside this range, the MS cannot be used for momentum measurements but can still detect the presence of muons.

To reduce the amount of data to be stored and analysed after the collisions, a dedicated system of triggers is needed. As the delivered luminosity grows, especially with the HL-LHC, the triggers need to be continuously improved. At ATLAS, the triggers are separated into multiple levels that each reduce the amount of data handled by the next one [39]. The first level trigger (L1) checks the events for objects with high transverse momenta or large missing transverse momentum. Based on the L1 decision, events are saved for further reconstruction at a rate up to 100 kHz [45]. Regions of interest in η and ϕ are identified by the L1 as well and provided to the High-Level Trigger (HLT) together with the recorded detector signal of each selected event. In this software based trigger, a further reconstruction of objects is performed in order to select interesting events. The output rate of the HLT was on average 1.2 kHz in Run 2 leading to 1.2 $\mathrm{GB\,s^{-1}}$ being saved for offline analyses [45]. Upgrades in preparation for Run 3 increased the granularity of the triggers and increased the output frequency to 3 kHz in accordance with the increased luminosity of the LHC [46].

3.3. Object Identification and Reconstruction

An electron's signature in the detector is a track in the ID and an energy deposition where the electron enters the ECAL. The identification of electrons in this analysis is done with a likelihood-based working point [47]. Electrons are required to satisfy the `MediumLH` requirement in order to be considered for the analysis. The isolation of electrons and photons is determined by measuring the energy $E_{\mathrm{T}}^{\mathrm{coneXX}}$ deposited in a cone of size $\Delta R = \frac{\mathrm{XX}}{100}$ around the particle in the ECAL. By subtracting the energy of the particle itself and applying some corrections from energy leakage and pileup, the energy surrounding the particle is found. Similarly, the momentum of tracks around a particle in the ID is defined as $p_T^{\mathrm{varconeXX}}$. The cone has a variable size that is fixed at $\Delta R = \frac{\mathrm{XX}}{100}$ for small momenta and becomes smaller for large transverse momenta.

For this analysis, a distinction is made between loosely and tightly selected electrons. The tight electrons require an isolation at the `Tight-VarRad` level, which is comprised of the following requirements [47]:

$$\frac{E_T^{\mathrm{cone20}}}{p_T} < 0.06 \quad \text{and} \quad \frac{p_T^{\mathrm{varcone30}}}{p_T} < 0.06\ .$$

No isolation criterion is applied to the loose electrons. To improve the quality of both types of electrons, some minimal kinematic cuts are applied. Since the track in the ID is important for electrons, only particles that pass the ID are to be considered. Particles with high pseudorapidities are therefore excluded. The space between the ID barrel and the end caps, also known as the crack region, is filled with inactive material and excluded as well. The resulting requirement is $|\eta| < 1.37$ or $1.52 < |\eta| < 2.47$. As electrons with low momenta are reconstructed with larger uncertainties and smaller purity, a cut of $p_{\mathrm{T}} > 7\,\mathrm{GeV}$ is applied.

Muons are minimum ionising particles at their energies observed in ATLAS, characterising their signature. They can leave tracks in the ID and pass through the calorimeters with little energy loss. In consequence, they are the only prompt particles that are expected to pass the calorimeters and leave hits in the MS. The main reconstruction method for muons is to combine a track in the MS with a matching one in the ID. In the `Medium` quality used for this analysis, the geometric acceptance is enlarged to the region $2.5 < |\eta| < 2.7$

by adding tracks only detected in the MS in this region as muons [48]. As for electrons, a minimum transverse momentum of 7 GeV is required for all muons. These tracks need to be matched to the primary interaction point in order to be considered. The isolation requirements are based on the same discriminants as for electrons [48]. Again, the tight definition includes the `Tight-VarRad` isolation, while the loose definition requires none.

Jets are mainly detected as energy deposited in the calorimeters and can include multiple tracks in the ID pointing toward the clusters. Combining these energy clusters into different jets is performed using the anti-k_t algorithm [49]. As most pileup events create jets, pileup removal is focused on jets as well. The kinematic constraints for jets are $p_\mathrm{T} > 25\,\mathrm{GeV}$ and $|\eta| < 4.5$. Jets found in the forward region with $2.5 < |\eta| < 4.5$ are called forward jets. The strategy used to remove pileup jets is to associate each jet to its primary vertex and then remove all jets not originating from the studied vertex. Assigning each jet to a vertex was done using the Neural Network Jet Vertex Tagger (NNJVT). This neural network is an improved version of the Jet Vertex Tagger [50] and was developed to be used in the high-pileup environment of the HL-LHC. For forward jets the specialised forward Jet Vertex Tagger is used [51], since the tracking information from the inner detector is missing.

Distinguishing b-jets from other jets is possible since the initial b-hadrons decay with a noticeable distance to the primary vertex. For this analysis, the neural network based algorithm `DL1r` is used for b-tagging [52, 53]. The b-tagging can be performed at different desired efficiencies. Choosing, for example, the 85 % working point means that 85 % of all true b-jets are b-tagged. A better purity can be reached by choosing lower efficiencies. Due to the missing tracking information, no b-tagging is applied to forward jets.

Neutrinos have tiny interaction cross-sections with matter, which means that large specialised detectors and a high neutrino flux are necessary to detect even a few neutrinos. A reliable neutrino detection in the ATLAS detector is therefore impossible. However, indirect measurements can be performed through conservation laws. As the colliding protons have no transverse momentum, the vector sum of all transverse momenta in the final state should add up to zero. In the case of a single neutrino in the final state, this does not hold true, as the neutrino's momentum is missing in this sum. Under the assumption that no other momenta have been ignored, the missing transverse energy can be assumed to correspond to the neutrino. This quantity $E_\mathrm{T}^\mathrm{miss}$ is defined as [54]:

$$\mathbf{E}_\mathrm{T}^\mathrm{miss} = - \sum_{i \in \{e.\mu,\tau,\gamma,\mathrm{jets}\}} \mathbf{p}_{\mathrm{T},i} - \sum_{j \in \{\text{unused tracks}\}} \mathbf{p}_{\mathrm{T},j} \ .$$

In this definition, it is important to only consider objects that pass the object selection and tracks associated with the same primary vertex. Without these requirements, energy and momentum from pileup events could be included in $E_{\mathrm{T}}^{\mathrm{miss}}$ and the assumption of zero transverse momentum no longer holds.

The object definitions presented in this section are "unaware" of the other definitions and may define multiple objects from the same tracks and clusters. To avoid double counting of particles, an overlap removal (OR) needs to be applied to the list of all objects. The inputs of the OR are the tight electrons and muons and all jets without accounting for b-tags. Effectively, the OR algorithm applies the following decisions one after another to all reconstructed objects:

First, any electron that shares its track with a muon is removed. Next, for each electron, a cone of $\Delta R = 0.2$ is constructed to remove all jets that fall within these cones. After this step, similar cones with $\Delta R = 0.4$ are constructed around the remaining jets in order to remove electrons that are likely parts of the jets. If a jet is within $\Delta R = 0.2$ of a muon, the number of tracks associated with the jet is considered as well. Jets that are associated with less than three tracks are removed. Lastly, muons are removed if they lie within $\Delta R = 0.4$ of one of the remaining jets.

4. Data and Simulated Events

To develop an analysis strategy and study the possible sensitivity to BSM effects, recorded data cannot be used to achieve an unbiased analysis. Additionally, the true process and final state underlying each recorded event are unknown in data. Instead, specially developed Monte Carlo (MC) generators are used to simulate events that resemble the true interactions happening at the LHC. The MC simulations usually start by calculating the Matrix Element corresponding to the desired production process. This step is followed by simulating the parton showering that occurs after the primary interactions and leads to the formation of composite particles and jets from bare quarks. Hadrons containing either charm or bottom quarks are characterised by their lifetime, leading to secondary decays at a macroscopic distance from the initial production vertex. The decays of these heavy flavour hadrons need to be simulated as well to obtain an accurate final state. These previous simulation steps are usually called the event generation.

In order to obtain a dataset similar to the recorded data, the interactions between the final state particles and the detector need to be simulated. This detector simulation is performed with either of the tools GEANT4 [55] or AtlFast3 [56]. Additionally, the electronic read-out system is simulated to finally obtain information in the same format as the data recorded in the detector. Starting from this step, analyses can be implemented that work equally on simulated events and data.

4.1. Data

This analysis uses data from Run 2 of the LHC lasting from 2015 to 2018. The integrated luminosity recorded in this dataset is $140.1 \pm 1.2\,\text{fb}^{-1}$ [57]. Multiple single-lepton triggers were used to record the data. In 2015 the trigger thresholds were set to momenta of $p_\text{T} = 24\,\text{GeV}$ and $120\,\text{GeV}$ for electrons and $p_\text{T} = 20\,\text{GeV}$ for muons [58]. Due to the increased luminosity in Run 2, the electron triggers were increased in 2016 to require $p_\text{T} = 26\,\text{GeV}$, $60\,\text{GeV}$ and $140\,\text{GeV}$ [59]. Similarly, the single-muon triggers were set to require $p_\text{T} = 26\,\text{GeV}$ and $50\,\text{GeV}$ [60].

4.2. Signal Processes

This analysis aims to study the effect of 5 EFT operators on trileptonic $t\bar{t}X$ final states. The relevant processes affected by these operators are $t\bar{t}Z$, tZq, and tWZ. For these processes, the production is modelled using MadGraph5_aMC@NLO [61] to compute the associated Matrix Elements at NLO and generate the MC events. The NLO PDFs used for these simulations are the NNPDF3.0NLO PDF set [62]. The parton showering is simulated with Pythia8 [63] using the A14 tune [64] and the NNPDF2.3LO PDF set [65]. Finally, EvtGen [66] is used to simulate the decay of hadrons containing b and c quarks in the final state.

As explained in Section 2.3, the 4FS or 5FS can be used to model the tZq production. For this analysis, the 4FS was chosen and all tZq events were simulated at NLO. In addition to $\ell^+\ell^-$pairs from Z decays, a small non-resonant contribution at lower energies is included in this sample as well.

As discussed in Section 2.3, the tWZ production process interferes with the $t\bar{t}Z$ production process at higher orders. To avoid double counting of events in both samples, overlapping diagrams and interference terms are removed in the matrix element calculation. The diagram removal scheme chosen for the simulation in this analysis is called DR1 [67].

The effects of SMEFT contributions on the signal processes are simulated by reweighting the events simulated based on the SM expectations. For this purpose, the SMEFTsim3.0 package [68, 69] was used as an extension for MadGraph5_aMC@NLO to include additional SMEFT effects in the Matrix Element calculation. The model *top* was used to include additional dimension-6 EFT operators that focus on interactions of the top quark. The resulting samples are simulated at LO in QCD and include alternative weights corresponding to varied Wilson coefficients.

4.3. Background Processes

Any non-signal process that leads to an identical final state is called a background process. The *Diboson* background consists of two vector bosons and additional jets from pileup interactions ($WZ +$jets or $ZZ +$jets) with the bosons decaying into three charged leptons and a neutrino, or four charged leptons. In the case of four charged leptons, the process can be mistaken for a trileptonic final state if one of the leptons is not detected or does not pass the reconstruction criteria. Events corresponding to this background were simulated at NLO using Sherpa 2.2.2 [70] and the NNPDF3.0NNLO PDF set.

Different processes consisting of a $t\bar{t}$ pair and an additional boson are listed as $t\bar{t}X$. In the case of an associated W boson, the dileptonic $t\bar{t}$ decay is required for a total of 3 charged leptons. These events are generated with Sherpa 2.2.12. Events corresponding to $t\bar{t}\gamma$ with the photon decaying into leptons are simulated using MadGraph5_aMC@NLO for the hard interaction. As for the signal processes, the parton showering is simulated using Pythia8, and EvtGen provides b- and c-decays. Another process in the $t\bar{t}X$ category is $t\bar{t}H$ with the hard scattering modelled through the POWHEG BOX 2 generator [71] with the NNPDF3.0NLO PDF set. Pythia8 and EvtGen are used again for parton showering and heavy flavour decays. Lastly, $t\bar{t}Z$ events with the decay modes $Z \to \tau^+\tau^-$ and $Z \to \nu\bar{\nu}$ could be falsely reconstructed with a trileptonic final state due to missed or non-prompt leptons. These events are simulated together with the above-mentioned $t\bar{t}Z$ signal samples.

Events characterised by the presence of non-prompt leptons are listed as *Fakes* in this analysis. The background of a dileptonically decaying $t\bar{t}$ system and a single non-prompt lepton is simulated through POWHEG Box 2 with Pythia8 parton showering and heavy flavour decays from EvtGen. A second contribution to the *Fakes* category are events with an on-shell Z boson, a non-prompt lepton and additional jets. These events are simulated with Sherpa 2.2.1 and the NNPDF3.0NNLO PDF set.

A source of non-prompt electrons that is not covered by these samples is the conversion of a prompt photon. The corresponding events containing a vector boson, a photon and additional jets are listed as $V\gamma + \text{jets}$. Sherpa 2.2.11 was used to simulate these events.

Any remaining rare processes that might appear in the trileptonic final state through misidentified objects are grouped as *Other* processes. The production of $t\bar{t}$ together with two W boson and three-top quark production ($tt\bar{t}$) are modelled at LO using MadGraph5_aMC@LO. Pythia8 is used with the A14 set of tuned parameters and the NNPDF2.3 PDF set to simulate the parton showering, followed by heavy flavour decays from EvtGen. *Diboson* production events with less than three charged leptons in the final states are simulated with Sherpa 2.2.1 with the NNPDF3.0NNLO PDF set. Similarly, events with three vector bosons are simulated in Sherpa 2.2.2 with the same PDF sets. The production of four top quarks ($t\bar{t}t\bar{t}$) is simulated similarly to the signal processes using MadGraph5_aMC@NLO, Pythia8, and EvtGen. The NNPDF3.1 PDF set is used for this sample. Lastly, the associated production of a vector boson and a Higgs boson (VH) is simulated in POWHEG, followed by Pythia8 with NNPDF3.0NLO PDFs and EvtGen.

5. Event Selection and Reconstruction

The decay of the Z boson into jets is hard to identify and reconstruct in a jet-rich environment as is found in the Atlas detector, and the invisible decay into neutrinos cannot be directly detected. Therefore, this analysis will focus on the decay into charged leptons ($Z \to \ell^+\ell^-$). For the $t\bar{t}$ system, choosing between the dileptonic, semi-leptonic, and fully hadronic decay modes is a trade-off between reconstruction quality and the number of available events. The reconstruction quality is generally highest for leptons compared to jets, while the branching ratio into jets is larger. In the case of single top quarks, the decision is between the leptonic or hadronic decay. By choosing the leptonic decay for the tZq process, a final state containing three leptons is obtained. In addition, this trileptonic final state contains one b-tagged jet from the top decay and an additional jet in the forward region. Since the production requires an initial state b quark arising from gluon splitting, an additional b jet may be found with a lower transverse momentum. The $t\bar{t}Z$ process can be studied in the same trileptonic region by assuming the semi-leptonic $t\bar{t}$-decay. Lastly, the tWZ production contains the additional W that can decay into a lepton and a neutrino or into jets. That way, a leptonic top decay or a leptonic W boson decay can lead to our trileptonic final state, assuming that the other particle decays hadronically.

5.1. Event selection

In order to study the signal processes $t\bar{t}Z$ and tZq, a set of selection criteria can be applied to all events. The goal of this selection is to reject events from background processes while keeping as many signal events as possible. A set of such criteria is often referred to as a signal region (SR). While signal regions are designed to contain a high purity of signal events, control regions (CR) can be used to estimate background contributions independent of the signal. Some selection criteria are applied as a preselection for all regions and serve to narrow down the studied final states. The preselection for the trileptonic final

Table 5.1.: Selection for trileptonic final states of $t\bar{t}Z$ and tZq sorted by top (e/μ+jets) and Z decay modes ($e^+e^-/\mu^+\mu^-$). The event selection is based on [25].

final state	$e+\text{jets}, e^+e^-$	$e+\text{jets}, \mu^+\mu^-$	$\mu+\text{jets}, e^+e^-$	$\mu+\text{jets}, \mu^+\mu^-$
N_e	$=3$	$=1$	$=2$	$=0$
N_μ	$=0$	$=2$	$=1$	$=3$
N_{OSSF}	≥ 1 with $\lvert m_{\ell\ell} - m_Z\rvert < 10\,\text{GeV}$			
N_{jets}	≥ 3			
N_{b-tag}	≥ 1 at 85%			

state in this analysis consists of the criteria listed in Table 5.1. The preselection is based on the selection used in the most recent ATLAS $t\bar{t}Z$ measurement [25] in the trileptonic final state. The preselection can be split into four sub-regions depending on the number of electrons and muons. These categories represent the permutations of the decay modes of the top quark and the Z boson. As discussed in Section 3.3, the b-tagging can be performed at different working points. For this signal region, the working point with the highest efficiency of 85 % is chosen in order to include as many events as possible.

Any process including a Z decaying into charged particles has a non-resonant background from photons with the same final state. Rejecting these events is achieved through another requirement on the kinematics of the leptons. The leptons are required to include at least one pair of opposite signs and the same flavour (OSSF). For this pair, the invariant mass, $m_{\ell\ell}$, is calculated by adding the four-momenta and computing the square. The mass is then required to be within a 10 GeV window around the Z mass $m_Z = 91.1876 \pm 0.0021\,\text{GeV}$ [11].

After applying the preselection, two signal regions and three control regions can be defined. The criteria defining these five regions are listed in Table 5.2. In tZq production, the second b-jet arises from gluon splitting and is expected to be found at a lower transverse momentum than b-jets from top quark decays. Since this soft b-jet is easily missed in the jet selection, typically only one b-tagged jet is found in tZq final states. As a consequence, requiring at least 2 b-jets leads to a region enriched in $t\bar{t}Z$ events. Unlike in tZq production, jets in *Diboson* events are not expected to show a preference for the forward region. This fact can be used to separate tZq from *Diboson* events by requiring at least one forward jet. The remaining significant group of background events are those with two prompt leptons and one non-prompt-lepton. Non-prompt leptons are commonly found with lower momentum than prompt leptons from top quark decays. As an OSSF pair near the Z boson mass is required for all events, those leptons are less likely to be

Table 5.2.: Signal and Control Regions used in this analysis. In addition to the preselection, this selection uses the multiplicity of b-jets and forward jets as well as the momentum and flavour of the lepton not belonging to an OSSF pair.

Region	SR ttZ	SR $t\ell\ell q$	CR Diboson	CR Fakes e	CR Fakes μ
N_{bjet}	> 1	$= 1$	$= 1$		
N_{fjet}		> 0	$= 0$		
$p_{\mathrm{T}}(\ell_{\text{non-}Z})$	> 20	> 20	> 20	≤ 20	≤ 20
$\ell_{\text{non-}Z}$ PDG-Id				$== 11$	$== 13$

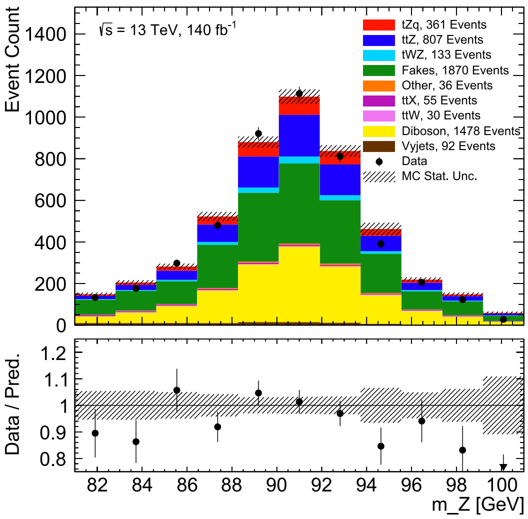

Figure 5.1.: Kinematic histograms of the Z mass reconstructed in signal and background processes in the trileptonic final state. Recorded data is shown for comparison.

non-prompt. The lepton that is not part of the Z boson decay is therefore required to have a minimum p_{T} of 20 GeV. Depending on the flavour of this non-prompt lepton, the events are separated between non-prompt electrons and non-prompt muons.

5.2. Z boson reconstruction

Reconstructing the Z boson starts with identifying the OSSF lepton pair the Z decays into. The invariant mass of all available OSSF pairs is computed to choose the pair closest to the Z mass. The resulting distribution of Z boson masses can be seen in Figure 5.1 in a comparison between signal and background processes and recorded data. Since a cut was imposed on the Z mass window, only values within $m_Z \pm 10\,\text{GeV}$ appear. By adding the four-momenta of these leptons, the four-momentum of the Z is obtained. After reconstructing the Z, it is important to exclude the lepton pair as candidates for future reconstruction steps.

5.3. Top decay reconstruction

The strategy chosen to reconstruct the top quarks depends on the number of top quarks in the process. For tZq production, the third lepton must be associated with the top quark. To reconstruct the top quark, the b-jet and the W are needed. If multiple b-jets are detected, the one with the highest p_T is chosen for the top reconstruction. When reconstructing the W decay, the transverse momentum of the neutrino can be estimated by $E_\mathrm{T}^\mathrm{miss}$ while the momentum in z-direction is unknown. This missing momentum can be calculated analytically, using the knowledge of the W mass $m_W = 80.377 \pm 0.012\,\mathrm{GeV}$ [11]. In the calculation of Equation (5.1), the masses of neutrinos, as well as electrons and muons, are neglected in comparison to the momenta of the particles.

$$m_W^2 = (p_\nu + p_\ell)^2 \approx 2p_\nu p_\ell \Leftrightarrow a \cdot p_{z,\nu}^2 + b \cdot p_{z,\nu} + c = 0 \tag{5.1}$$

$$\begin{aligned} a &= p_{z,\ell}^2 - E_\ell^2 \ , \\ b &= 2\ p_{z,\ell} \left(\frac{1}{2} m_W^2 + \vec{p}_{T,\ell} \cdot \vec{p}_{T,\mathrm{miss}} \right) \ , \\ c &= \left(\frac{1}{2} m_W^2 + \vec{p}_{T,\ell} \cdot \vec{p}_{T,\mathrm{miss}} \right)^2 - E_\ell^2\ \vec{p}_{T,\mathrm{miss}}^{\,2} \ . \end{aligned} \tag{5.2}$$

The above equation can be solved with the quadratic formula:

$$p_{z,\nu} = \frac{-b \pm \sqrt{b^2 - 4ac}}{2a} \ .$$

If two solutions exist for $p_{z,\nu}$, the more central one is chosen. Should the solutions be complex, the real part is used. With the assumption of negligible neutrino masses, the neutrino four-momentum can be estimated and used to reconstruct the W. Adding the b-jet to the W yields the top quark four-momentum.

In $t\bar{t}Z$ production, only one top quark decays leptonically. The association of jets to the top quarks can be done by using a Symmetry Preserving Attention Network (SPANet) [72]. Other approaches to calculating the likelihood of each possible assignment require a lot of computing power due to the many possibilities. Especially in final states involving multiple jets, the number of combinations grows quickly. This type of neural network avoids checking the permutations of jets by using the set of all jets as the input to a

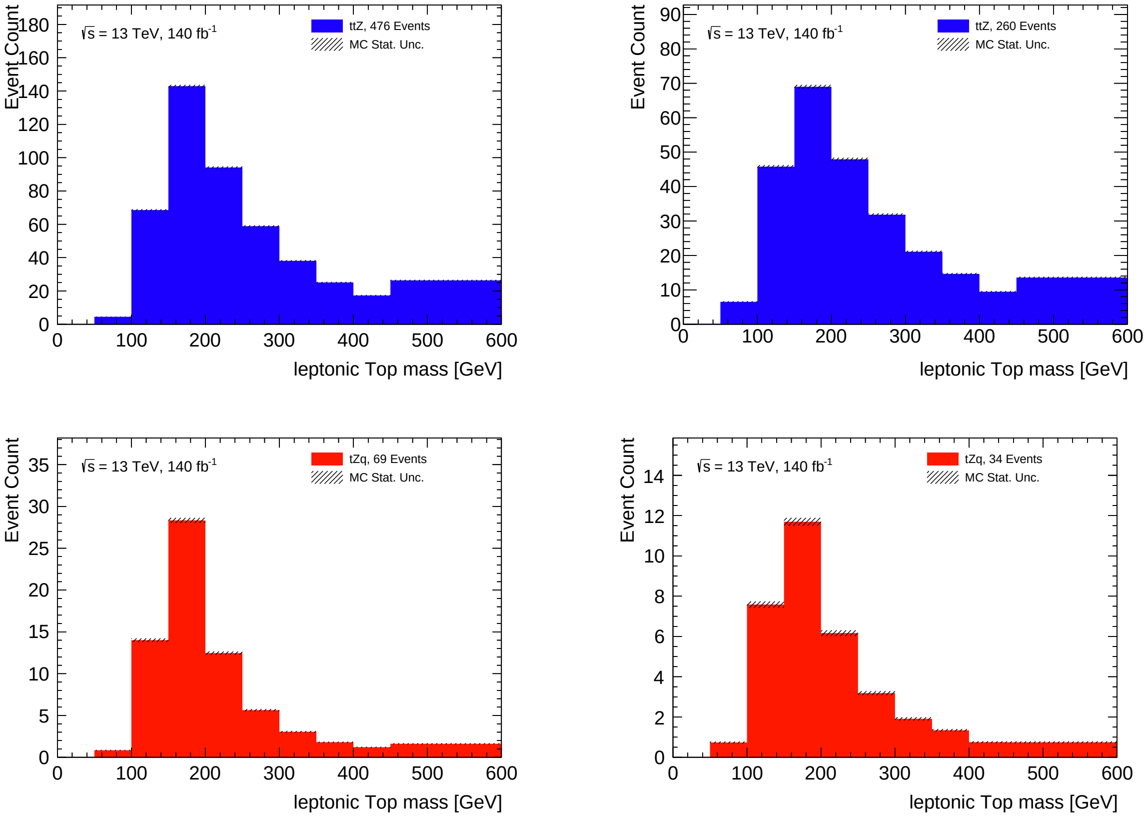

Figure 5.2.: Histograms of the reconstructed top quark mass are shown for (top) $t\bar{t}Z$ production and (bottom) tZq production. For each process, the mass is reconstructed using the leading b-jet and the W mass (left) and via the SPANet assignment (right).

transformer that predicts the most likely assignment. Special care is taken to avoid double counting of particles. Exchanged particles that do not affect the reconstruction are still considered as correctly assigned in training. An example of this is the reconstruction of a W decaying into jets. As jet charges are generally not measured at ATLAS, the quark and antiquark jets cannot be separated and lead to the same reconstructed W. The SPANet architecture was first applied to $t\bar{t}$ production in 2020 [73] and generalised to other topologies in 2022. In this analysis, a version of SPANet trained on semileptonic $t\bar{t}$ production is used. If multiple leptons are present in the final state, the leading electron is used per default and the leading muon if no electrons are detected. Since a lepton assignment to the Z boson is done in this analysis, only the remaining lepton is passed to SPANet to avoid double counting a lepton. Recently, a regression method to find the neutrino's momentum was added to SPANet [74]. The output of this SPANet setup is the information on which jets belong to each top quark and the momentum of the neutrino. Simple additions of the jet, lepton, and neutrino four-momenta yield the four-momentum of each top quark.

The masses of the reconstructed particles can be compared to study the performance of both reconstruction methods. For the $t\bar{t}Z$ and tZq samples the reconstruction strategies are compared side-by-side in Figure 5.2. Each process is analysed in the corresponding signal region as defined in Section 5.1.

The mass distributions found in both samples have their peak in the 150 GeV to 200 GeV bin that contains the expected top quark mass. Notably, the distribution is rather wide compared to the expected mass peak with a width of only $1.42^{+0.19}_{-0.15}$ GeV [11]. In conclusion, the observed widths are dominated by the chosen reconstruction strategy and the resolution of the ATLAS detector. Additionally, the distribution has a tail of higher masses that do not agree with a correct reconstruction. Since this tail is more pronounced for $t\bar{t}Z$ events, it might correspond to wrongly assigned b-jets that should belong to the hadronically decaying top quark. Another possible problem in the reconstruction of $t\bar{t}Z$ events is that the event selection allows for events that contain less than four jets. In such events, the full reconstruction of the $t\bar{t}$ system is impossible. Roughly 36 % of all $t\bar{t}Z$ events fall into this category.Using the reconstruction strategy without the SPANet assignment leads to more reconstructed top quarks since all events contain at least one b-jet. Many of these additional top quarks are, however, missing their correct b-jet and should ideally not be reconstructed. Consequently, choosing the reconstruction strategy according to the signal region is a good strategy to obtain reconstructed top quarks if they are to be used in further cuts or fits.

6. Fitting

6.1. Profile Likelihood Fitting

The probability of measuring a result $\mathbf{n}$ given a set of parameters $\boldsymbol{\theta}$ can be described by a likelihood function $L(\mathbf{n}|\boldsymbol{\theta})$. Maximising this likelihood leads to the best parameter values $\hat{\boldsymbol{\theta}}$ for describing the measurement. The logarithm of the likelihood function is often maximised instead, leading to an improved performance.

Usually, in fits, one of the parameters is the parameter of interest μ, while the other parameters are called nuisance parameters. To express the likelihood only in terms of μ, the profile likelihood $\lambda(\mathbf{n}|\mu)$ can be used:

$$\lambda\left(\mathbf{n}\,|\,\mu\right) = \frac{L\left(\mathbf{n}\,\middle|\,\mu, \hat{\hat{\boldsymbol{\theta}}}\right)}{L\left(\mathbf{n}\,\middle|\,\hat{\mu}, \hat{\boldsymbol{\theta}}\right)}\,. \tag{6.1}$$

In this formula, $\hat{\hat{\boldsymbol{\theta}}}$ are the best-fit nuisance parameters from a fit with μ being fixed. The profile likelihood is normalised to a maximum of 1 for μ being identical to the best-fit value $\hat{\mu}$ and it gets close to 0 for unlikely values of μ.

6.2. Template histograms

A probability distribution for a binned variable x is described through a template histogram. In such a histogram, the expected number of events $E[n_i]$ in a bin i is the sum of the expected background events b_i and the signal events $s_i(\mu)$ influenced by some parameter μ. The expectation values are influenced by uncertainties in the modelling accounted for through the nuisance parameters. Any measurement can be described through its event counts $\mathbf{n}$ in all N bins. The number of events within each bin follows a Poisson distribution around the expected value. Additional measurements $\mathbf{m}$ independent of μ can be used to constrain the nuisance parameters. The likelihood function for a template histogram with constrained nuisance parameters is:

$$L\left(\mathbf{n},\mathbf{m}\,|\,\mu,\boldsymbol{\theta}\right)=\prod_{j=1}^{N}\frac{\left(s_j(\mu,\boldsymbol{\theta})+b_j(\boldsymbol{\theta})\right)^{n_j}}{n_j!}e^{-(s_j(\mu,\boldsymbol{\theta})+b_j(\boldsymbol{\theta}))}\cdot\prod_{k=1}^{M}\frac{u_k^{m_k}(\boldsymbol{\theta})}{m_k!}e^{-u_k(\boldsymbol{\theta})}\ . \tag{6.2}$$

6.3. Hypothesis tests

In particle physics, the usual goal is to study some hypothesis of new physical phenomena compared to the SM prediction. The decision whether to accept or reject a null hypothesis H_0 in favour of an alternative hypothesis H_1 is made via hypothesis testing. The hypotheses can be expressed as $\mu = 0$ for an SM-only-hypothesis and $\mu \neq 0$ for an additional-effect-hypothesis. For excluding new effects, the test statistic t_μ can be used [75]:

$$t_\mu = -2\log(\lambda(\mu))\ . \tag{6.3}$$

This quantity becomes large for λ being close to 0, corresponding to a disagreement between the model and the measurement.
The probability of finding a disagreement with H_0 of at least $t_{\mu,\text{obs}}$ if H_0 were true is the p-value as seen in (6.4). To compute the p-value, the probability distribution function of t_μ must be known. Asymptotic formulae for such pdfs in the case of many events are provided in [75].

$$p_\mu = \int_{t_{\mu,\text{obs}}}^{\infty} f\left(t_\mu|\mu\right)\mathrm{d}t_\mu\ . \tag{6.4}$$

As a measure for excluding a hypothesis, the confidence level CL of excluding any value μ can be calculated as seen in (6.5). For a given level CL, the values that are not excluded from the corresponding confidence interval. The typically studied confidence levels are CL $\leq$ 68 % and CL $\leq$ 95 %. This quantity is a relation between a test's significance $\alpha = p_\mu$ and its exclusion potential $1-\beta$.

$$\mathrm{CL}(\mu) = \frac{\int_{t_{\mu,\text{obs}}}^{\infty} f\left(t_\mu|\mu\right)\mathrm{d}t_\mu}{\int_{t_{\mu,\text{obs}}}^{\infty} f\left(t_\mu|0\right)\mathrm{d}t_\mu} = \frac{\alpha}{1-\beta}\ . \tag{6.5}$$

7. Analysis

The goal of this analysis is to search for BSM effects through SMEFT. To achieve this goal, a workflow is needed to process simulated and recorded events into histograms. These histograms can then be used as the input for fits to obtain Wilson coefficients. As preparation for fits with recorded data, the fits can be performed with Asimov data identical to the SM prediction. While these fits should lead to resulting Wilson coefficients of 0, the uncertainties can be used to estimate the sensitivity to possible effects.

7.1. Analysis Overview

For this analysis, profile likelihood fitting is chosen as the method for measuring BSM effects. The fits are performed using both the SM expectation and histograms including SMEFT contributions as template histograms. The first steps of the analysis are to create a set of simulated events from all relevant processes and apply the preselection. Reconstruction can be applied to this dataset. Finally, the dataset is split into different regions, and histograms can be produced. The histograms should be produced for all systematic variations to obtain systematic uncertainties in the final fitting result. Similarly, the SMEFT contribution histograms are produced. The profile likelihood fits for all relevant Wilson coefficients are performed using the histograms. For global SMEFT searches, many Wilson coefficients are included, leading to many degrees of freedom that require at least as many bins in the fit. This can be achieved by using many selection categories to gain more final bins. Previous analyses from ATLAS and CMS used about 50 signal categories with a single bin for the total yield each [76, 77]. Producing these large numbers of histograms is a time consuming step of SMEFT searches. In total, about 75 signal and background samples are used in this analysis with three MC campaigns as described in Chapter 4 and listed in Appendix A.2. In Section 7.5, the roughly 350 systematic variations are discussed. Multiplying the total number of bins in signal categories with the variations results in about 17.5 thousand bins filled with the events of all samples.

7.2. Ntuple Production

Most analyses use events saved as tabular data called `ntuples` in the `TTree` format native to ROOT [78]. These files are created from larger derived Analysis Object Data (DAOD) files. In preparation for the growing event numbers expected to be recorded at the HL-LHC by ATLAS, the centralised `DAOD_PHYS` and `DAOD_PHYSLITE` formats were introduced [79]. Using large central files reduces disk space usage from duplicates and similar samples. Another advantage of using a standard format is the ability to process the files with the same software framework. In another centralisation effort, the algorithms developed by the combined performance (CP) groups are now applied as common CP algorithms. These algorithms are used for many steps in event preparation common to most analyses. Important examples are the application of systematic variations and scale factors to the events. Additionally, object definitions can be passed to the algorithms that create lists of all objects and perform the overlap removal. Some event selection decisions can be implemented in this step as well. These decisions are based on object multiplicities, flavour tagging, momenta, charges, and even invariant masses. Advantages of centralised software are a reduced risk of bugs and the chance to improve the performance by focusing on a smaller set of algorithms.

The `TopCPToolkit` is a newly developed framework using common CP algorithms to produce `ntuples` from DAODs. The framework was first released to the ATLAS community in August of 2023. As a consequence, this analysis is among the first to utilise the framework and verify the improved performance. The development of or contribution to `TopCPToolkit` was not part of this thesis. In addition to the common CP algorithms, `TopCPToolkit` contains algorithms specific to top quark physics and the possibility to add custom algorithms. Top specific algorithms include the implementation of SPANet for the jet assignment in semileptonic $t\bar{t}$ decays. As this version of SPANet was trained on samples containing a single lepton, it simply uses the highest p_{T} lepton for the top reconstruction. Therefore, it is essential to label the leptons from the Z decay and ignore them for the top reconstruction. A custom algorithm was written for this purpose, finding the respective leptons according to Section 5.2. Generally, custom algorithms are used to produce `ntuples` best suited for each individual analysis.

The output `ntuples` of `TopCPToolkit` follow the single `TTree` format. In this format, systematic variations of variables are saved as additional branches in a single `TTree`. Compared to the previously used format that added an entire `TTree` per systematic, this format saves disk space by avoiding duplicate variables. Additionally, only one loop is needed to process all variations saving computing time and resources.

All samples used in this analysis were processed using `TopCPToolkit`. The respective dataset identifiers (DSIDs) are listed in Appendix A.2 and correspond to the processes described in Chapter 4. The time needed for processing the samples on the world Lhc computing grid (WLCG) is in the order of a few hours when running without systematic variations. Including the systematic variations, the computing time grows to roughly 1 to 2 days. Due to failing jobs and the necessary retries, the workflow can take around 4 to 5 days until the last sample is successfully processed.

7.3. Histogramming

Using the `ntuples`, various kinematic variables can be represented as histograms. For this purpose, the `ntuples` are read into the `RDataFrame` format [80]. The new columnar format treats each event as a line in a table with one column per variable. New columns can be calculated from existing ones. The code for calculating the new columns is in-time compiled `C++`-code which allows `RDataFrames` to reach the performance of `C++` code while being used in `python`. This improvement of the computing time is an important step towards the analyses of large HL-Lhc datasets. In addition, `RDataFrames` use lazy execution to avoid calculating variables that are not used in any histogram or similar result. `RDataFrames` have an automatic handling of systematic variations included. Each column is defined in the `*_NOSYS` version without any variation. The code then applies only those variations that impact the column and creates all necessary additional columns. The reprocessing and histograming in this analysis was performed with the tool `FastFrames` that was recently developed to further process `ntuples` produced by `TopCPToolkit`. Like for `TopCPToolkit`, this tool was not developed as part of this thesis but is used in order to study the viability of these new tools for Run 3.

Reprocessing the `ntuples` to perform the reconstruction of the Z boson and the top quark according to Sections 5.2 and 5.3 takes about 30 min on a local machine when run without systematics. Including the systematics required switching to distributed computing and processing all samples in parallel. This way, the run time ended up at roughly 8 h for the largest samples. A benchmark of the histogramming performance was done on a single CPU core of a local machine with the results shown in Figure 7.1. For this benchmark, events belonging to the $ttZ(\rightarrow ee)$ process were used with all systematic variations. Both, the number of produced histograms and the number of events used were varied to study their effect on computing time. While varying the number of histograms, 105 k events were used. The resulting behaviour is linear for many histograms. For few tens to hundreds of histograms, the computing time grows slightly slower than a linear function. This hints at some overhead possibly due to reading files that is more relevant when producing few histograms.

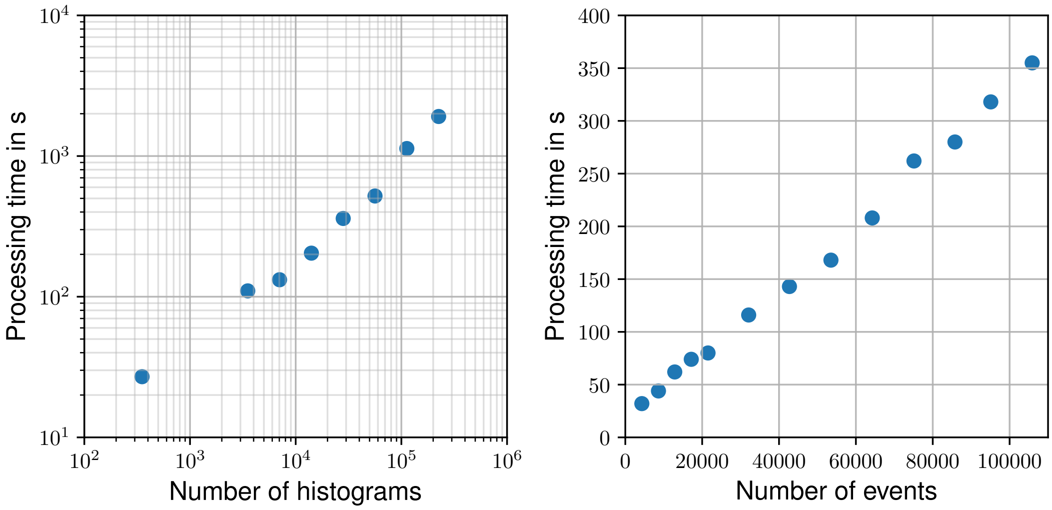

Figure 7.1.: Results of a histogramming benchmark in `FastFrames` run on a single CPU core. The dependence on (left) number of histograms and (right) number of events was investigated.

40 histograms were produced for each of the roughly 350 systematic variations while using different numbers of events. This behaviour is linear. With the dependency of computing time on these two variables known, the necessary time to produce the final histograms can be estimated. Assuming samples to have an average number of events equivalent to the $t\bar{t}Z$ samples, one obtains a total of roughly 19 million events. These events are filled into each of the estimated 17.5 k histograms. This corresponds to a time of 200 s multiplied by 225 to account for the additional samples. As a result, one can expect the histogramming with all systematic variations to take around 12 h on a local machine.

This expectation did not prove to be true when performing the histogramming for all samples, including systematics. Since many samples consist of multiple DSIDs, the time needed to read metadata scaled worse than expected. Similarly, the time needed to create and write multiple small files is not proportional to the number of events in them. As a consequence, the histogramming was parallelised like the reprocessing of the `ntuples`. This way, the time needed to process the largest sample was reduced to just 5 h.

7.4. Data vs. MC examination

Histograms produced via `FastFrames` can be used to compare the kinematic distribution of signal and background events to the distribution of recorded data. As examples, stacked histograms are shown in Figure 7.2. The left histogram shows the transverse momentum of the lepton that is not part of the OSSF pair and thus assumed to be produced

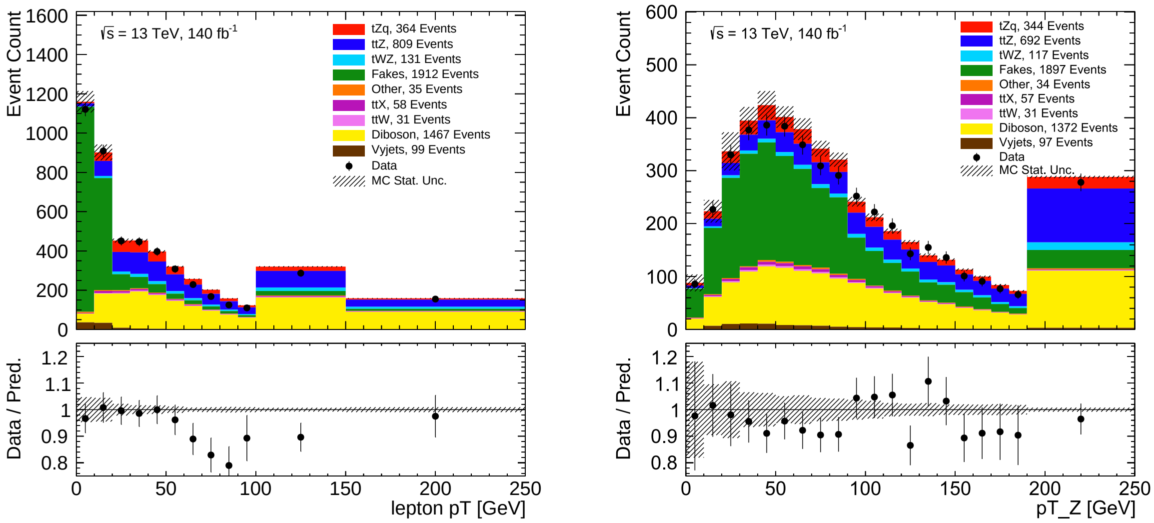

Figure 7.2.: Kinematic histograms of signal and background processes in the trileptonic final state. The transverse momenta of (left) the lepton not belonging to the Z decay and (right) of the Z boson are shown. Recorded data is shown for comparison.

in the top decay. A bit more than a third of all data points lie outside the uncertainty of the MC prediction. Since the uncertainties shown in this histogram are only statistical, including systematic uncertainties might still improve the agreement. However, a third of all data points are always expected to lie outside the 1σ interval.

The transverse momentum of the reconstructed Z bosons can be seen in the right histogram. The agreement between the MC prediction and the data is good, with the predicted value covered by the data's uncertainty in two thirds of the bins. In both distributions, the difference in event count between $t\bar{t}Z$, tZq, and tWZ is clearly visible. The tZq events are much rarer than $t\bar{t}Z$, and their distribution might be better studied in a signal region enriched in tZq events. Both histograms clearly show that the most relevant background processes in this signal category are *Diboson* production process and processes including non-prompt leptons (*Fakes*). The leptons in the *Fakes* categories are characterised by their small momentum, which is visible in the distribution on the left. *Diboson* events follow a distribution much more similar to the $t\bar{t}Z$ and tZq events. In the distribution of the reconstructed Z mass, the $t\bar{t}Z$, *Diboson*, and *Fakes* show a similar behaviour as all of these processes include real Z bosons. Backgrounds without Z bosons are rejected through the mass window requirement on the OSSF lepton pair.

These distributions can be used to develop the region definitions shown in Section 5.1. The *Fakes* category is separated from the other events through a cut on the transverse momentum of the lepton. A further distinction can be made between non-prompt elec-

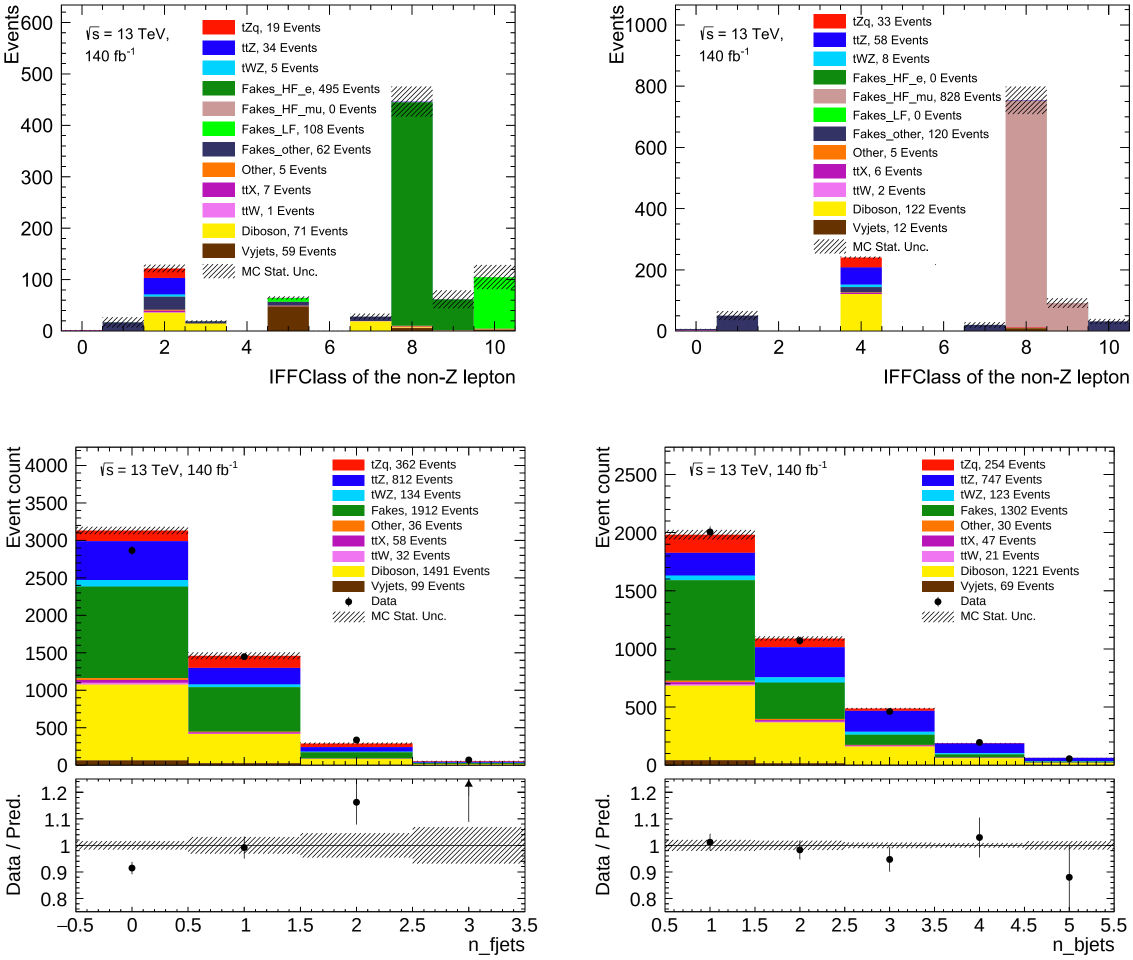

Figure 7.3.: IFF classes to distinguish between Fake-types are shown in the Fakes-e (top left) and Fakes-μ control regions (top right). The number of forward jets (lower left) and b-tagged jets (lower right) are additional important variables in distinguishing signal and control regions.

trons and muons since these are produced in different ways. The source of non-prompt leptons is recorded in MC-simulated samples in classes defined by the Isolation and Fake Forum (IFF) working group. In Figure 7.3, these IFF classes are shown for the two regions CR Fakes e and CR Fakes μ.

The IFF classes 0 and 1 denote that the type of non-prompt lepton was not determined. Events placed in the following bins contain prompt electrons (2), electrons with a misidentified charge (3), or prompt muons (4). Additional sources of fake electrons are prompt photons (5) or decaying light-flavour hadrons (10). Decay particles from hadronic τ decays (7), b decays (8), or c decays (9) can be mistaken for either prompt electrons or muons. If an electron is misidentified as a prompt muon, the associated class is 6.

As discussed in Section 5.1, the splitting between the $t\bar{t}Z$ and tZq signal regions and the

Diboson control region is performed using the multiplicity of b-tagged and forward jets. The distributions for both variables before splitting into regions is shown in Figure 7.3. In the distribution of forward jets, the number of tZq events with at least one forward jet is similar to those without, while the *Diboson* background decreases. Similarly, about half of all $t\bar{t}Z$ events occur with two b-jets, while all backgrounds dramatically decrease. This ensures a very clean region for $t\bar{t}Z$ and some separation between tZq and *Diboson*.

7.5. Systematic Uncertainties

All events, either simulated or recorded at Atlas, are affected by systematic uncertainties. Some uncertainties affect parts of the simulation of processes, like the parton distribution functions. Other uncertainties result from incomplete knowledge of the detector resolution and affect recorded data as well as the simulated events. The uncertainties are usually taken into account by varying the affected parameter by one standard deviation upward and downward to produce systematic variations of the resulting events. The treatment of these variations can account for a lot of resource usage and should, therefore, be handled efficiently, as discussed in the previous sections. Any modelling uncertainties, like the choice of MC generators and PDFs, were not implemented in this analysis. Instead, only experimental uncertainties have been considered, resulting in 262 variations applied to the events.

The simulated pileup events for each sample need to be reweighted to match the distributions found in data. This process results in the pileup reweighting scale factor.

The electron selection is affected by the efficiencies associated with the identification, isolation, reconstruction, and triggers [81]. The uncertainty of each efficiency is split into a correlated and an uncorrelated component. In total 81 nuisance parameters (NPs) are included to correspond to these electron efficiency uncertainties.

The corresponding efficiency for muons is affected by uncertainties on the isolation, reconstruction, and triggers as well. Additionally, the track-to-vertex-association is performed for muons, leading to uncertainties on the efficiency [48]. These uncertainties are represented by 36 NPs.

Besides the efficiencies, the energy and momentum values obtained for electrons and muons are associated with uncertainties. For electrons and photons, the energy scale and resolution uncertainties are represented through one NP each. In muons, one NP corresponds to the momentum scale. Additionally, the sagitta bias influences the momentum with its uncertainty split into four NPs.

In the definition of $E_{\mathrm{T}}^{\mathrm{miss}}$, soft tracks are considered in addition to other objects like leptons and jets. A scale factor corrects the energy scale of these soft tracks to match data. This scale factor's uncertainty corresponds to another NP.

Due to the importance of b-tagging, the efficiency of flavour tagging can greatly influence the reconstruction of an event. Different efficiency uncertainties are found depending on a jet's true flavour. These corrections lead to a total of 87 NPs.

The energy measurement of jets depends on the jet energy scale (JES) and the jet energy resolution (JER) [82, 83]. Corrections are applied to the JES to account for changes due to flavour, pseudorapidity, pileup, and detector geometry. Additionally, smaller effects are summarised into effective corrections. The JER is accounted for in the detector through in-situ calibrations and by comparison to data. In total, JES and JER are taken into account through 47 NPs. Similarly to the efficiencies for electrons and muons, the pileup rejection efficiency through the NNJVT and fJVT has 2 NPs to account for the uncertainties.

7.6. SMEFT Fitting

The effect of SMEFT variations, as simulated with the `SMEFTsim` package, can be expressed through the equation:

$$N_{\text{SMEFT}} = N_{\text{SM}} + \sum_i c_i A_i + \sum_{i,j} c_i c_j B_{i,j} \ . \tag{7.1}$$

In this calculation, N is the number of expected events based on either the SM or SMEFT. A_i quantifies the interference effects between SM diagrams and a SMEFT operator $\mathcal{O}_i$. As introduced in Section 2.4, the Wilson coefficient c_i is a parameter corresponding to the strength of $\mathcal{O}_i$. The pure SMEFT contribution of either one or multiple SMEFT operators is given through $B_{i,j}$. Using the EFT MC samples, a quadratic fit can be performed for every Wilson coefficient to obtain the corresponding A_i and $B_{i,i}$. Similarly, every combination of two different coefficients can be used in a fit to obtain the interference terms $B_{i,j}$. With these parameters known, the event counts N_{SMEFT} from signal processes can be expressed as functions of the Wilson coefficients c_i. In summary, the parameters of interest are c_i, while the normalisation factors of background processes remain as nuisance parameters. Finally, a template histogram fit as described in Section 6.2 can be performed to estimate the Wilson coefficients.

Samples containing SMEFT variations are generated at LO, while samples based on the SM expectation are generated at NLO. This generally leads to a difference in a process's total cross-section and event count. The SMEFT varied histograms are reweighted to

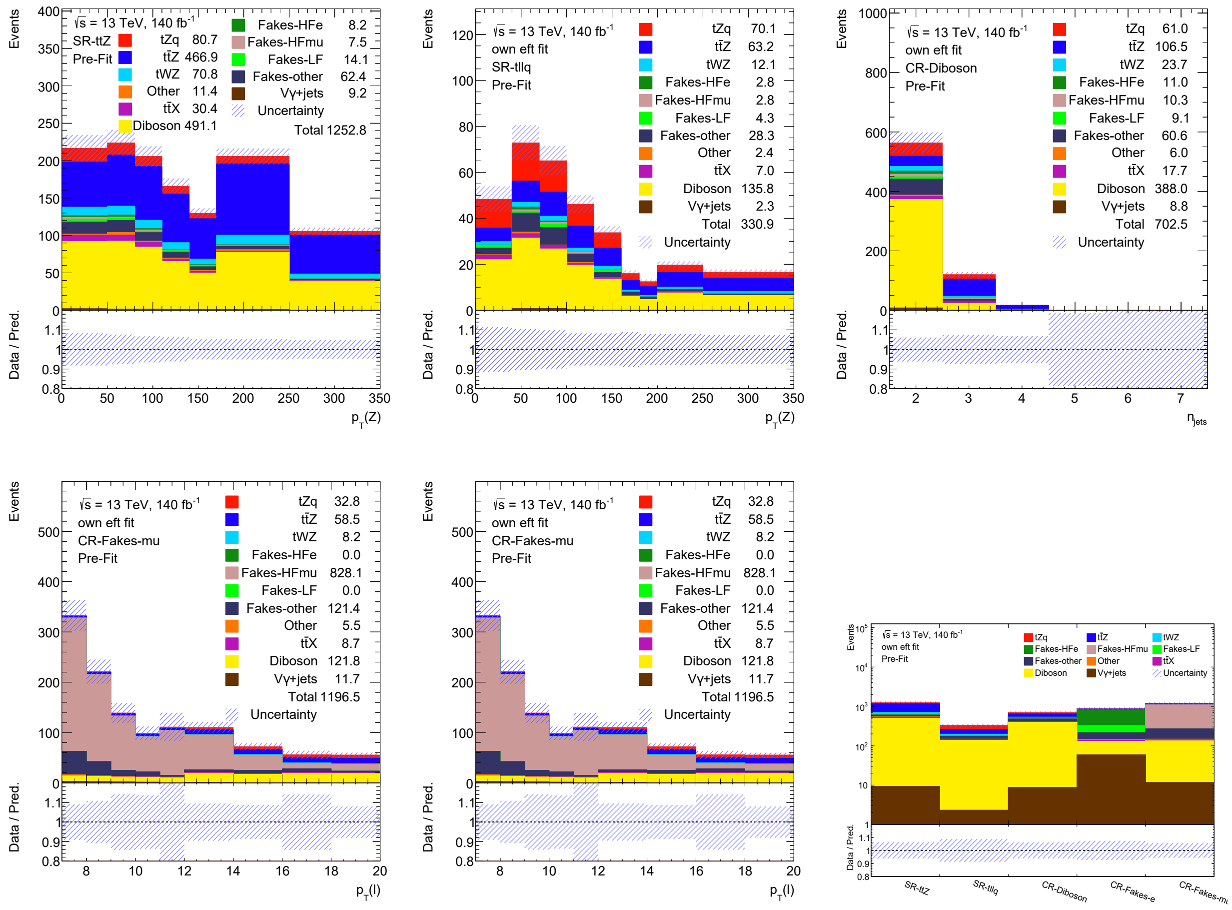

Figure 7.4.: Input histograms used for the EFT fit in `TRExFitter`. The Z boson p_T is shown in the signal regions for $t\bar{t}Z$ (top left) and tZq (top middle). In the control regions, the jet multiplicity is shown for *Diboson* events (top right). The p_T of the non-Z lepton is used for the *Fakes-e* (bottom left) and *Fakes-μ* (bottom middle) regions. The summary plot (bottom right) shows the total event count in each region.

the NLO cross-section to correct this difference. The underlying assumption is that the relative effect from SMEFT variations is the same at LO and NLO.

Since this analysis focuses on the trileptonic final state, the possibility of having many signal regions is limited. To obtain enough bins to perform the fit, kinematic distributions with multiple bins were chosen as an input in each region instead of total cross-sections. In $t\bar{t}Z$ and tZq production, the interaction between the top quark and the Z boson might be affected by BSM effects. As shown in Section 2.4, such effects grow with the transverse momentum of the Z boson. To gain sensitivity on such effects, the transverse momentum $p_{\mathrm{T},Z}$ of the reconstructed Z boson was chosen as the input histogram in both signal regions. The choice of the binning in these histograms is important because bins with too few events lead to increased statistical uncertainty in the results. At the same time, choosing too few bins makes the histogram less sensitive to shape variations, which also leads to less sensitive results to some BSM effects. The binning for this analysis was chosen by hand and is shown in Figure 7.4, including systematic uncertainties. These histograms do not contain data in order to perform Asimov fits. Therefore, the ratio plot only shows relative uncertainties for each bin. Different variables can be chosen in the control regions, as these are not expected to be sensitive to the SMEFT variations. For the two *Fakes* regions, the transverse momentum $p_{\mathrm{T},\ell}$ of the non-Z lepton is used. The Diboson region is split into bins according to the jet multiplicity. In addition to the five regions, a summary histogram gives the total event count in each region.

The fit setup consists of one Wilson coefficient as the parameter of interest and five normalisation factors corresponding to the signal processes and the largest background categories. A bin normalisation factor is added to account for the statistical uncertainty for each bin in the histograms. Systematic uncertainties with an influence below a threshold of 0.7 % are not included in the fit. The remaining uncertainties are included through 173 additional nuisance parameters. This setup was used to independently study the five Wilson coefficients c_{Ht}, $c_{HQ}^{(1)}$, $c_{HQ}^{(3)}$, $c_{tB}^{(\mathrm{Re})}$, and $c_{tB}^{(\mathrm{Re})}$. As seen introduced in Section 2.4, these operators affect the interaction between the top quark and the Z boson.

The first step of the fit is determining the values A_i and $B_{i,i}$ for the given Wilson coefficient as described above. This is achieved through a quadratic fit in each bin of the relative SMEFT effect as a function of the Wilson coefficient. The results of this fit in the $t\bar{t}Z$ signal region for different values of c_{Ht} can be seen in Figure 7.5. In addition to these fits, the last plots show the relative change of linear and quadratic terms due to c_{Ht} in each bin. Similar plots that were obtained in fits to all five Wilson coefficients are shown in Appendix A.3. For $t\bar{t}Z$ production, the effect of c_{Ht} on the cross-section is strongest and appears mostly linear corresponding to an interference with the SM. The plots of relative changes confirm that the effect on $t\bar{t}Z$ is also largest relative to the large cross-section. The effect on tZq events is weaker and associated with large uncertainties, possibly due to the low event count. In tWZ events, an effect of similar magnitude to tZq can be observed with smaller uncertainties. The relative change for both linear and quadratic terms shows that the relative effect on tWZ is larger than on tZq but still much smaller than the effect on $t\bar{t}Z$. The resulting curves in all processes clearly show that the influence of c_{Ht} is larger for events involving high p_{T} Z bosons.

Based on these parameters A_i and $B_{i,i}$, a likelihood scan can be performed for different values of the Wilson coefficient. The resulting likelihood in Figure 7.6 is expected to be minimal at a value of zero in an Asimov fit. It can be used to obtain the uncertainty of

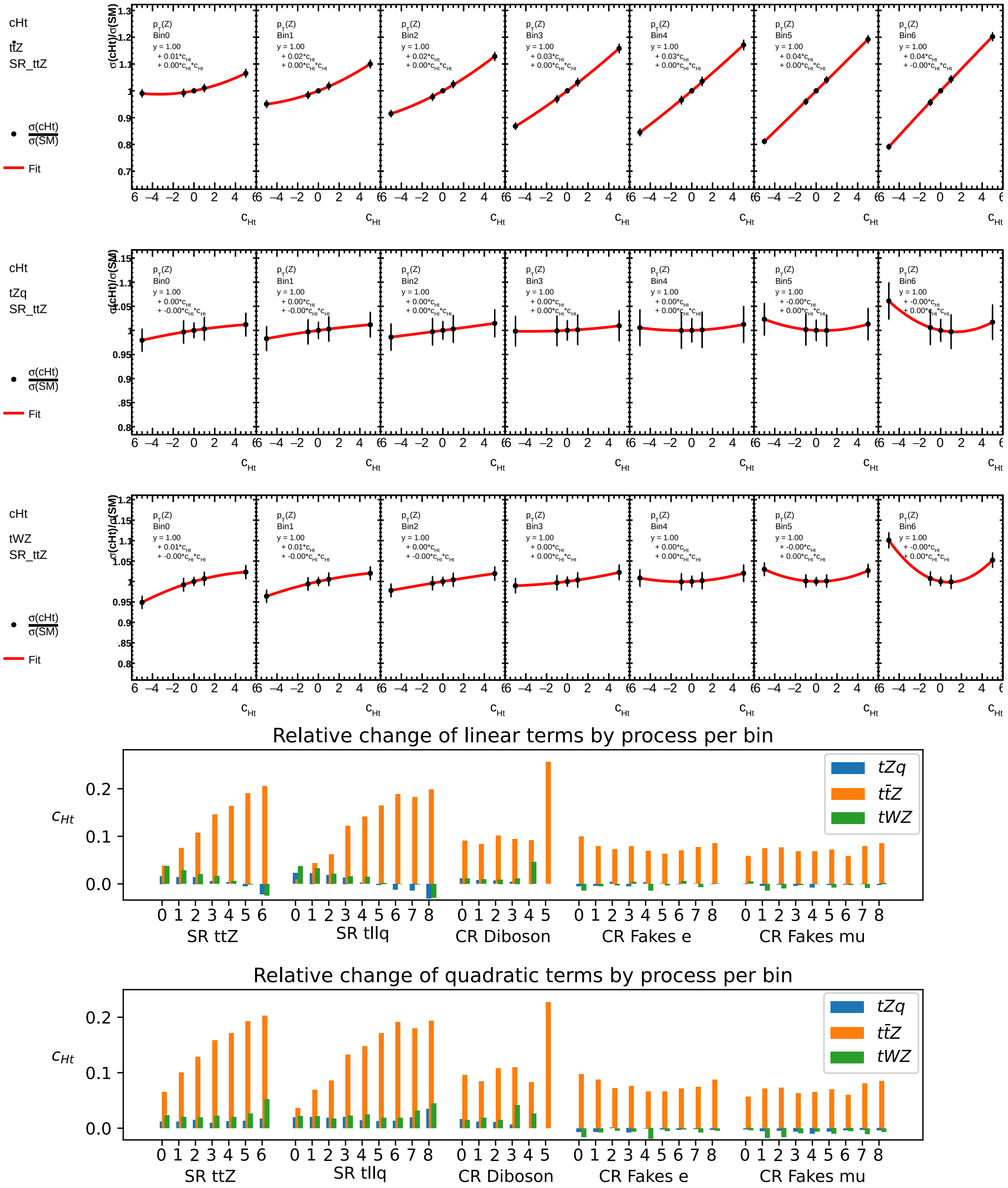

Figure 7.5.: Results of the quadratic fit performed in each bin to parametrize the effect of the Wilson coefficient c_{Ht}. The shown plots are obtained in the $t\bar{t}Z$ signal region for the processes $t\bar{t}Z$ (first), tZq (second) and tWZ (third). Additionally, the relative changes of linear (fourth) and quadratic (fifth) terms due to c_{Ht} are shown.

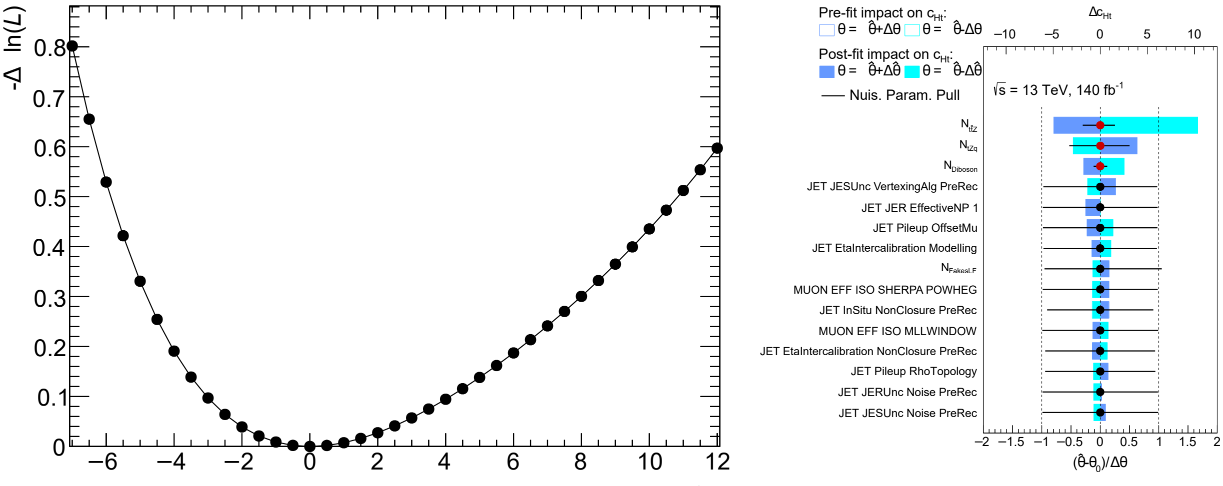

Figure 7.6.: Likelihood scan for different values of the Wilson coefficient c_{Ht} (left). Additionally, the impact of the 15 most influential nuisance parameters is shown (right).

Table 7.1.: The values for the Wilson coefficient and all normalisation factors obtained from the fits to each Wilson coefficient.

Wilson coefficient	Best-fit value
c_{Ht}	$0.00^{+10.28}_{-4.61}$ (stat.)$^{+3.45}_{-3.64}$ (syst.)
$c_{HQ}^{(1)}$	$0.00^{+4.80}_{-22.61}$ (stat.)$^{+5.77}_{-8.34}$ (syst.)
$c_{HQ}^{(3)}$	$0.00^{+3.82}_{-1.34}$ (stat.)$^{+0.90}_{-1.26}$ (syst.)
$c_{tB}^{(\mathrm{Re})}$	$0.00^{+2.14}_{-2.19}$ (stat.)$^{+0.04}_{-0.04}$ (syst.)
$c_{tW}^{(\mathrm{Re})}$	$0.00^{+0.84}_{-0.81}$ (stat.)$^{+0.28}_{-0.29}$ (syst.)

the Wilson coefficient as seen in Table 7.1. Due to the linear effect c_{Ht} has on $t\bar{t}Z$ production, negative values will decrease the event count. This leads to a numerical limit in the fit when the yield becomes zero and explains the asymmetric bounds seen in Figure 7.6. Additionally, the impact of the 15 most influential nuisance parameters is ranked in the right plot. Most of these nuisance parameters refer to systematic uncertainties in the detection and reconstruction of jets. While the likelihood scan and nuisance parameters for each Wilson coefficient are shown in Appendix A.3, the resulting Wilson coefficients are listed in Table 7.1. These results are clearly dominated by statistic uncertainty, and more work is needed before the fits can be performed on data.

In addition to the effect a single Wilson coefficient has on the event count, there are also interference effects between different SMEFT operators. The search for such effects can be done by simulating weights for the case of two non-zero Wilson coefficients. With these samples, both Wilson coefficients can be treated as floating parameters of interest

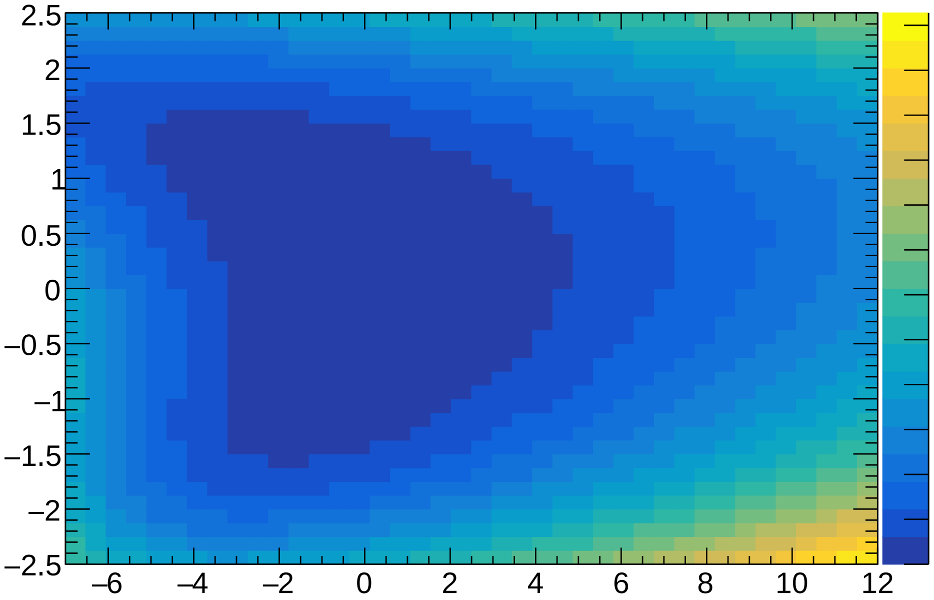

Figure 7.7.: Two dimensional likelihood of the Wilson coefficients c_{Ht} and $c_{tB}^{(\mathrm{Re})}$.

in the fit while all other coefficients are still fixed at zero. Including interference terms can help reduce the uncertainty, while adding another floating parameter increases the degree of freedom in the fit. Based on the results from single coefficient fits, the simultaneous search for two varied coefficients is not expected to yield more precise results. The two dimensional likelihood for c_{Ht} and $c_{tB}^{(\mathrm{Re})}$ is shown in Figure 7.7. While the exclusion of large values for c_{Ht} is still rather weak, the likelihood for $c_{tB}^{(\mathrm{Re})}$ becomes much narrower for those values. The area of non-excluded values is not shaped like an ellipse as would be expected for independent variables. This illustrates how the phase space of combinations $(c_{Ht}, c_{tB}^{(\mathrm{Re})})$ is reduced by the simultaneous fit.

8. Conclusion and Outlook

An essential part of this analysis is to use state-of-the-art software developed in preparation for future analyses. This way, potential bugs or missing features can be discovered early to ensure fast and efficient usage when it is needed to process the large datasets of future runs. The successful creation of `ntuples` with a small computing time as discussed in Section 7.2 is proof that `TopCPToolkit` is a viable tool to perform analyses on the `DAOD_PHYS` derivation format.
Similarly, the histogramming in `FastFrames` shows both the usability of the framework and the performance achieved by relying on the `RDataFrames`. This framework is very flexible through the use of custom `C++` algorithms to define branches. Through this feature, the reconstruction of the top quarks was performed. As shown in Section 7.3, the reconstruction is performed in a reasonable timescale as well. While the estimated 12 h for histogramming based on a single sample proved too optimistic, the parallelisation option led to an overall reduced time. With 35 processes running in parallel, the duration was lowered to just 5 h. This duration is determined by the longest-running samples, which are the signal samples including the EFT variations. Many of the other processes finish much faster, with 15 processes taking less than 1 h. Combined with the reprocessing of `ntuples`, where the longest process takes around 8 h, the part of this workflow performed in FastFrames takes less than a day to complete. The two steps of reprocessing and histogramming were split in this analysis for the purpose of flexibility while designing the analysis. Once all regions and desired histograms are defined, both steps can be performed simultaneously, eliminating the need to read and write all events twice. An additional speed-up is to be expected from this change.

The Wilson coefficients obtained through EFT fits in this analysis are dominated by their large statistical uncertainties. For the SMEFT search in the future $t\bar{t}X$-multilepton analysis, these uncertainties need to be reduced as much as possible. A major improvement over this analysis would be to include more processes as signals with dedicated regions. While the focus was set on $t\bar{t}Z$, tZq, and tWZ for this analysis, other processes like $t\bar{t}H$ and $t\bar{t}W$ could be included. These processes are generally affected by the Wilson coefficients in different degrees. This leads to the opportunity of both a decreased uncertainty and the search for other Wilson coefficients. When including new processes, one would necessarily include signal regions that offer a high purity of these events and thus increase the number of input bins for the EFT fits.

Another benefit of additional regions and processes is the opportunity to improve the background estimation for the *Fakes* category. The current approach of separating events based on the lepton transverse momentum is very sensitive to the p_{T} distribution of non-prompt leptons. These distributions are hard to study and simulate accurately. If the distribution were shifted towards higher p_{T} values, many events would be missing from the dedicated regions. As a result, the fit would lead to a reduced normalisation factor for this category. Therefore, the contribution of these events in the signal regions would be estimated to be smaller while it is actually increased compared to the prediction. The solution to this problem is to choose different control regions. While OSSF pairs are required for the signal regions, non-prompt leptons are often studied in events with same-sign same-flavour (SSSF) pairs or three same-sign leptons instead. These lepton combinations do not occur as decay products of a resonant particle and are thus well suited to study non-prompt leptons. This analysis did not implement such a region as it was excluded from the preselection. In a more general analysis a looser preselection is already necessary to include more processes and no trade off is necessary between small datasets and a better estimation of non-prompt leptons.

In terms of improving the resolution with the studied processes, the separation between the different signals could be improved. The distinction between $t\bar{t}Z$, tZq, and the *Diboson* background can be greatly improved through the use of a deep neural network for classification. While beyond the scope of this thesis, both `TopCPToolkit` and `FastFrames` offer an interface for the use of neural networks in the Open Neural Network Exchange (ONNX) format. Another possible direction for improvements is further searches for kinematic variables sensitive to different SMEFT operators. While operators that affect $t\bar{t}Z$ have a strong effect on the Z boson p_{T}, other variables might get better results depending on the studied Wilson coefficient.

If a more sensitive selection and fit are achieved, an additional fit can be performed, where all studied Wilson coefficients are treated as parameters of interest and fitted simultaneously. While this is the most demanding fit in its degree of freedom and necessary inputs, it would include all available information from interference effects.

In comparing the SM expectation histograms with those including SMEFT variations, the critical assumption was made that the relative EFT contribution to a process is identical at LO and NLO. This is not true for all combinations of processes and coefficients. In a process that is propagated purely through the strong interaction at LO, for example, an electroweak contribution might be added at NLO. Such an electroweak interaction is generally sensitive to different coefficients compared to strong interactions, changing the relative contributions.

Bibliography

[1] R. Wideröe, *Über ein neues Prinzip zur Herstellung hoher Spannungen*, Arch. Elektrotech. **21**, 387 (1928)

[2] I. Zurbano Fernandez, et al., *High-Luminosity Large Hadron Collider (HL-LHC): Technical design report*, Technical Report CERN-2020-010, CERN (2020)

[3] CMS Collaboration, *Search for physics beyond the standard model in top quark production with additional leptons in the context of effective field theory*, JHEP **12**, 068 (2023)

[4] S. Weinberg, *The Making of the standard model*, Eur. Phys. J. C **34**, 5 (2004)

[5] S. Hannestad, *Dark energy and dark matter from cosmological observations*, Int. J. Mod. Phys. A **21**, 1938 (2006)

[6] A. D. Sakharov, *Violation of CP Invariance, C asymmetry, and baryon asymmetry of the universe*, Pisma Zh. Eksp. Teor. Fiz. **5**, 32 (1967)

[7] LHCb Collaboration, *Observation of $J/\psi\phi$ structures consistent with exotic states from amplitude analysis of $B^+ \to J/\psi\phi K^+$ decays*, Phys. Rev. Lett. **118(2)**, 022003 (2017)

[8] LHCb Collaboration, *Amplitude analysis of $B^+ \to J/\psi\phi K^+$ decays*, Phys. Rev. D **95(1)**, 012002 (2017)

[9] LHCb Collaboration, *Observation of $J/\psi p$ Resonances Consistent with Pentaquark States in $\Lambda_b^0 \to J/\psi K^- p$ Decays*, Phys. Rev. Lett. **115**, 072001 (2015)

[10] LHCb Collaboration, *Observation of a narrow pentaquark state, $P_c(4312)^+$, and of two-peak structure of the $P_c(4450)^+$*, Phys. Rev. Lett. **122(22)**, 222001 (2019)

[11] P. D. Group, *Review of Particle Physics*, PTEP **2022**, 083C01 (2022)

[12] S. L. Glashow, *Partial Symmetries of Weak Interactions*, Nucl. Phys. **22**, 579 (1961)

[13] S. Weinberg, *A Model of Leptons*, Phys. Rev. Lett. **19**, 1264 (1967)

[14] A. Salam, *Weak and Electromagnetic Interactions*, Proceedings of the eighth Nobel symposium **680519**, 367 (1968)

[15] F. Englert, R. Brout, *Broken Symmetry and the Mass of Gauge Vector Mesons*, Phys. Rev. Lett. **13**, 321 (1964)

[16] P. W. Higgs, *Broken symmetries, massless particles and gauge fields*, Phys. Lett. **12**, 132 (1964)

[17] P. W. Higgs, *Broken Symmetries and the Masses of Gauge Bosons*, Phys. Rev. Lett. **13**, 508 (1964)

[18] G. S. Guralnik, C. R. Hagen, T. W. B. Kibble, *Global Conservation Laws and Massless Particles*, Phys. Rev. Lett. **13**, 585 (1964)

[19] M. Kobayashi, T. Maskawa, *CP Violation in the Renormalizable Theory of Weak Interaction*, Prog. Theor. Phys. **49**, 652 (1973)

[20] M. Gell-Mann, *A Schematic Model of Baryons and Mesons*, Phys. Lett. **8**, 214 (1964)

[21] H. Fritzsch, M. Gell-Mann, H. Leutwyler, *Advantages of the Color Octet Gluon Picture*, Phys. Lett. B **47**, 365 (1973)

[22] CDF Collaboration, *Observation of top quark production in $\bar{p}p$ collisions*, Phys. Rev. Lett. **74**, 2626 (1995)

[23] DØ Collaboration, *Observation of the top quark*, Phys. Rev. Lett. **74**, 2632 (1995)

[24] A. Kulesza, et al., *Associated production of a top quark pair with a heavy electroweak gauge boson at NLO+NNLL accuracy*, Eur. Phys. J. C **79(3)**, 249 (2019)

[25] ATLAS Collaboration, *Inclusive and differential cross-section measurements of $t\bar{t}Z$ production in pp collisions at $\sqrt{s} = 13$ TeV with the ATLAS detector, including EFT and spin-correlation interpretations*, CERN-EP-2023-252 (2023)

[26] CMS Collaboration, *Measurement of top quark pair production in association with a Z boson in proton-proton collisions at $\sqrt{s} =$ 13 TeV*, JHEP **03**, 056 (2020)

[27] ATLAS Collaboration, *Observation of the associated production of a top quark and a Z boson in pp collisions at $\sqrt{s} = 13$ TeV with the ATLAS detector*, JHEP **07**, 124 (2020)

[28] CMS Collaboration, *Inclusive and differential cross section measurements of single top quark production in association with a Z boson in proton-proton collisions at* $\sqrt{s} = 13$ *TeV*, JHEP **02**, 107 (2022)

[29] ATLAS Collaboration, *Modelling Wt and tWZ production at NLO for ATLAS analyses*, in *9th International Workshop on Top Quark Physics* (2016)

[30] CMS Collaboration, *Evidence for tWZ production in proton-proton collisions at s=13 TeV in multilepton final states*, Phys. Lett. B **855**, 138815 (2024)

[31] CMS Collaboration, *Precision measurement of the W boson decay branching fractions in proton-proton collisions at $\sqrt{s}$ = 13 TeV*, Phys. Rev. D **105(7)**, 072008 (2022)

[32] ALEPH, DELPHI, L3, OPAL, SLD Collaborations, LEP Electroweak Working Group, SLD Electroweak Group, SLD Heavy Flavour Group, *Precision electroweak measurements on the Z resonance*, Phys. Rep. **427**, 257 (2006)

[33] S. Rao, R. E. Shrock, *Six Fermion $(B - L)$ Violating Operators of Arbitrary Generational Structure*, Nucl. Phys. B **232**, 143 (1984)

[34] C. Degrande, et al., *Effective Field Theory: A Modern Approach to Anomalous Couplings*, Annals Phys. **335**, 21 (2013)

[35] J. Ellis, et al., *Top, Higgs, Diboson and Electroweak Fit to the Standard Model Effective Field Theory*, JHEP **04**, 279 (2021)

[36] B. Grzadkowski, et al., *Dimension-Six Terms in the Standard Model Lagrangian*, JHEP **10**, 085 (2010)

[37] J. A. Aguilar-Saavedra, *A Minimal set of top anomalous couplings*, Nucl. Phys. B **812**, 181 (2009)

[38] L. Evans, P. Bryant, *LHC Machine*, JINST **3**, S08001 (2008)

[39] ATLAS Collaboration, *The ATLAS Experiment at the CERN Large Hadron Collider*, JINST **3**, S08003 (2008)

[40] ALICE Collaboration, *The ALICE experiment at the CERN LHC*, JINST **3**, S08002 (2008)

[41] CMS Collaboration, *The CMS Experiment at the CERN LHC*, JINST **3**, S08004 (2008)

[42] LHCb Collaboration, *The LHCb Detector at the LHC*, JINST **3**, S08005 (2008)

[43] T. Kawamoto, et al., *New Small Wheel Technical Design Report*, Technical report, CERN (2013)

[44] ATLAS Collaboration, *The New Small Wheel upgrade project of the ATLAS Experiment*, PoS EPS-HEP2021 page 756 (2022)

[45] ATLAS Collaboration, *Operation of the ATLAS trigger system in Run 2*, JINST **15**, P10004 (2020)

[46] ATLAS Collaboration, *The ATLAS Trigger System for LHC Run 3 and Trigger performance in 2022*, CERN-EP-2023-299 (2024)

[47] ATLAS Collaboration, *Electron and photon performance measurements with the ATLAS detector using the 2015-2017 LHC proton-proton collision data*, JINST **14**, P12006 (2019)

[48] ATLAS Collaboration, *Muon reconstruction performance of the ATLAS detector in proton-proton collision data at $\sqrt{s} = 13$ TeV*, Eur. Phys. J. C **76**, 292 (2016)

[49] M. Cacciari, G. P. Salam, G. Soyez, *The anti-k_t jet clustering algorithm*, JHEP **04**, 063 (2008)

[50] ATLAS Collaboration, *Performance of pile-up mitigation techniques for jets in pp collisions at $\sqrt{s} = 8$ TeV using the ATLAS detector*, Eur. Phys. J. C **76(11)**, 581 (2016)

[51] ATLAS Collaboration, *Forward jet vertex tagging using the particle flow algorithm*, ATL-PHYS-PUB-2019-026, Geneva (2019)

[52] ATLAS Collaboration, *Optimisation and performance studies of the ATLAS b-tagging algorithms for the 2017-18 LHC run*, ATL-PHYS-PUB-2017-013 (2017)

[53] ATLAS Collaboration, *ATLAS flavour-tagging algorithms for the LHC Run 2 pp collision dataset*, Eur. Phys. J. C **83(7)**, 681 (2023)

[54] ATLAS Collaboration, *Performance of missing transverse momentum reconstruction with the ATLAS detector using proton-proton collisions at $\sqrt{s} = 13$ TeV*, Eur. Phys. J. C **78**, 903 (2018)

[55] J. Allison, et al., *GEANT4 - a simulation toolkit*, Nucl. Instr. Meth. A **506(3)**, 250 (2003)

[56] ATLAS Collaboration, *AtlFast3: The Next Generation of Fast Simulation in ATLAS*, Comput. Softw. Big Sci. **6(1)**, 7 (2022)

[57] ATLAS Collaboration, *Luminosity determination in pp collisions at* $\sqrt{s} = 13$ *TeV using the ATLAS detector at the LHC*, Eur. Phys. J. C **83(10)**, 982 (2023)

[58] ATLAS Collaboration, *Performance of the ATLAS Trigger System in 2015*, Eur. Phys. J. C **77(5)**, 317 (2017)

[59] ATLAS Collaboration, *Performance of electron and photon triggers in ATLAS during LHC Run 2*, Eur. Phys. J. C **80(1)**, 47 (2020)

[60] ATLAS Collaboration, *Performance of the ATLAS muon triggers in Run 2*, JINST **15(09)**, P09015 (2020)

[61] J. Alwall, et al., *The automated computation of tree-level and next-to-leading order differential cross sections, and their matching to parton shower simulations*, JHEP **07**, 079 (2014)

[62] R. D. Ball, et al. (NNPDF), *Parton distributions for the LHC Run II*, JHEP **04**, 040 (2015)

[63] T. Sjöstrand, et al., *An introduction to PYTHIA 8.2*, Comput. Phys. Commun. **191**, 159 (2015)

[64] ATLAS Collaboration, *ATLAS Pythia 8 tunes to 7 TeV data*, Technical report, CERN, Geneva (2014), URL `https://cds.cern.ch/record/1966419`

[65] R. D. Ball, et al., *Parton distributions with LHC data*, Nucl. Phys. B **867**, 244 (2013)

[66] D. J. Lange, *The EvtGen particle decay simulation package*, Nucl. Instrum. Meth. A **462**, 152 (2001)

[67] S. Frixione, et al., *Single-top hadroproduction in association with a* W *boson*, JHEP **07**, 029 (2008)

[68] I. Brivio, Y. Jiang, M. Trott, *The SMEFTsim package, theory and tools*, JHEP **12**, 070 (2017)

[69] I. Brivio, *SMEFTsim 3.0 — a practical guide*, JHEP **04**, 073 (2021)

[70] E. Bothmann, et al. (Sherpa), *Event Generation with Sherpa 2.2*, SciPost Phys. **7(3)**, 034 (2019)

[71] S. Alioli, et al., *A general framework for implementing NLO calculations in shower Monte Carlo programs: the POWHEG BOX*, JHEP **06**, 043 (2010)

[72] A. Shmakov, et al., *SPANet: Generalized permutationless set assignment for particle physics using symmetry preserving attention*, SciPost Phys. **12(5)**, 178 (2022)

[73] M. J. Fenton, et al., *Permutationless many-jet event reconstruction with symmetry preserving attention networks*, Phys. Rev. D **105(11)**, 112008 (2022)

[74] M. J. Fenton, et al., *Reconstruction of Unstable Heavy Particles Using Deep Symmetry-Preserving Attention Networks* (2023)

[75] G. Cowan, et al., *Asymptotic formulae for likelihood-based tests of new physics*, Eur. Phys. J. C **71**, 1554 (2011), [Erratum: Eur.Phys.J.C 73, 2501 (2013)]

[76] Atlas Collaboration, *Measurement of the total and differential cross-sections of* $t\bar{t}W$ *production in pp collisions at* $\sqrt{s} = 13$ *TeV with the ATLAS detector*, CERN-EP-2023-260 (2024)

[77] Cms Collaboration, *Search for physics beyond the standard model in top quark production with additional leptons in the context of effective field theory*, JHEP **12**, 068 (2023)

[78] R. Brun, F. Rademakers, *ROOT - An object oriented data analysis framework*, Nucl. Instr. Meth. A **389(1)**, 81 (1997), new Computing Techniques in Physics Research V

[79] J. Elmsheuser, et al., *Evolution of the Atlas analysis model for Run-3 and prospects for HL-Lhc*, EPJ Web Conf. **245**, 06014 (2020)

[80] G. Amadio, et al., *Novel functional and distributed approaches to data analysis available in ROOT*, J. Phys. Conf. Ser. **1085(4)**, 042008 (2018)

[81] Atlas Collaboration, *Electron and photon energy calibration with the ATLAS detector using LHC Run 2 data*, JINST **19(02)**, P02009 (2024)

[82] Atlas Collaboration, *Jet Calibration and Systematic Uncertainties for Jets Reconstructed in the ATLAS Detector at* $\sqrt{s} = 13$ *TeV*, Technical report, CERN, Geneva (2015)

[83] Atlas Collaboration, *Jet energy scale and resolution measured in proton–proton collisions at* $\sqrt{s} = 13$ *TeV with the ATLAS detector*, Eur. Phys. J. C **81(8)**, 689 (2021)

A. Appendix

A.1. Systematic Variations

Object	Uncertainty name	N	Description
Event generation	`GEN_PDF__260XXX_NNPDF30_nlo_as_0118`	101	Parton distribution function
	`GEN_dyn__1_muR0X0000E0X_muF0X0000E0X`	9	Dynamic renormalisation (R) and factorization (F) scales
Jets	`JET_BJES_Response`	2	b-jet energy scale
	`JET_EffectiveNP_DetectorX`	4	Energy scale nuisance parameters from different sources
	`JET_EffectiveNP_MixedX`	6	
	`JET_EffectiveNP_ModellingX`	8	
	`JET_EffectiveNP_StatisticalX`	12	
	`JET_EtaIntercalibration_Modelling`	2	η dependency of energy scale
	`JET_EtaIntercalibration_NonClosure_PreRec`	2	
	`JET_EtaIntercalibration_TotalStat`	2	
	`JET_Flavor_Composition`	2	Flavour dependency of energy scale
	`JET_Flavor_Response`	2	
	`JET_InSitu_NonClosure_PreRec`	2	In-situ calibration effects on energy scale
	`JET_JERUnc_Noise_PreRec`	2	Energy resolution noise contribution
	`JET_JERUnc_Noise_PreRec_PseudoData`	2	
	`JET_JERUnc_mc20vsmc21_MC20_PreRec`	2	Simulation capaign effect on energy resolution
	`JET_JERUnc_mc20vsmc21_MC20_PreRec_PseudoData`	2	
	`JET_JER_DataVsMC_MC16`	2	Energy resolution from Data-MC comparison
	`JET_JER_DataVsMC_MC16_PseudoData`	2	
	`JET_JER_EffectiveNP_X`	24	Energy resolution nuisance parameters
	`JET_JER_EffectiveNP_X_PseudoData`	24	
	`JET_JESUnc_Noise_PreRec`	2	Noise contribution to energy scale
	`JET_JESUnc_VertexAlg_PreRec`	2	Vertex algorithm effect on energy scale
	`JET_JESUnc_mc20vsmc21_MC20_PreRec`	2	Simulation capaign effect on energy scale
	`JET_NNJvtEfficiency`	2	Efficiency of the NeuralNetwork-Jet-Vertex-Tagger
	`JET_Pileup_OffsetMu`	2	Pileup effects on the energy scale
	`JET_Pileup_OffsetNPV`	2	
	`JET_Pileup_PtTerm`	2	
	`JET_Pileup_RhoTopology`	2	
	`JET_PunchThrough_MC16`	2	Energy scale of jets propagating beyond the calorimeters
	`JET_SingleParticleHighPt`	2	Energy scale of high-p_{T} jets

Flavour tagging	`FT_EFF_B_systematics`	2	Efficiency in b-, c-, and light-flavour-tagging
	`FT_EFF_C_systematics`	2	
	`FT_EFF_Light_systematics`	2	
	`FT_EFF_extrapolation`	2	Extrapolation to high p_{T}-jets
	`FT_EFF_extrapolation_from_charm`	2	
Missing transverse energy	`MET_SoftTrk_ResoPara`	1	Resolution effects of unused tracks
	`MET_SoftTrk_ResoPerp`	1	
	`MET_SoftTrk_Scale`	2	Scale effects of unused tracks
Electrons	`EG_RESOLUTION_ALL`	2	Energy resolution
	`EG_SCALE_AF2`	2	Energy scale
	`EG_SCALE_ALL`	2	
	`EL_EFF_ID_TOTAL_1NPCOR_PLUS_UNCOR`	2	Identification efficiency
	`EL_EFF_Iso_TOTAL_1NPCOR_PLUS_UNCOR`	2	Isolation efficiency
	`EL_EFF_Reco_TOTAL_1NPCOR_PLUS_UNCOR`	2	Reconstruction efficiency
	`EL_EFF_TriggerEff_TOTAL_1NPCOR_PLUS_UNCOR`	2	Trigger efficiency
Muons	`MUON_EFF_ISO_BKGFRACTION`	2	Isolation efficiency effects
	`MUON_EFF_ISO_DRMUJ`	2	
	`MUON_EFF_ISO_LUMIUNCERT`	2	
	`MUON_EFF_ISO_MCXSEC`	2	
	`MUON_EFF_ISO_MLLWINDOW`	2	
	`MUON_EFF_ISO_QCDTEMPLATE`	2	
	`MUON_EFF_ISO_SHERPA_POWHEG`	2	
	`MUON_EFF_ISO_STAT`	2	
	`MUON_EFF_ISO_SUPRESSIONSCALE`	2	
	`MUON_EFF_RECO_BKGFRACTION`	2	Reconstruction and identification efficiency effects
	`MUON_EFF_RECO_CRX`	6	
	`MUON_EFF_RECO_FITMODEL_LOWPT`	2	
	`MUON_EFF_RECO_HIGHETA_PROBEIP`	2	
	`MUON_EFF_RECO_HIGHETA_PROBEISO`	2	
	`MUON_EFF_RECO_LUMIUNCERT`	2	
	`MUON_EFF_RECO_MATCHING`	2	
	`MUON_EFF_RECO_MATCHING_LOWPT`	2	
	`MUON_EFF_RECO_MCXSEC`	2	
	`MUON_EFF_RECO_PTDEPENDENCY`	2	
	`MUON_EFF_RECO_QCDTEMPLATE`	2	
	`MUON_EFF_RECO_STAT`	2	
	`MUON_EFF_RECO_STAT_LOWPT`	2	
	`MUON_EFF_RECO_SUPRESSIONSCALE`	2	
	`MUON_EFF_RECO_TAGPT`	2	
	`MUON_EFF_RECO_TRUTH`	2	
	`MUON_EFF_RECO_TRUTH_LOWPT`	2	

Muons	`MUON_EFF_TTVA_BKGFRACTION`	2	Track-to-vertex association efficiency effects
	`MUON_EFF_TTVA_LUMIUNCERT`	2	
	`MUON_EFF_TTVA_MCXSEC`	2	
	`MUON_EFF_TTVA_QCDTEMPLATE`	2	
	`MUON_EFF_TTVA_STAT`	2	
	`MUON_EFF_TTVA_SUPRESSIONSCALE`	2	
	`MUON_EFF_TrigStatUncertainty`	2	Trigger efficiency
	`MUON_EFF_TrigSystUncertainty`	2	
	`MUON_ID`	2	Momentum measurement in the ID and MS
	`MUON_MS`	2	
	`MUON_SAGITTA_DATASTAT`	2	Charge dependent momentum scale
	`MUON_SAGITTA_GLOBAL`	2	
	`MUON_SAGITTA_PTEXTRA`	2	
	`MUON_SAGITTA_RESBIAS`	2	
	`MUON_SCALE`	2	Energy scale
Pileup	`PRW_DATASF`	2	Pileup reweighting of events

Table A.1.: List all systematic uncertainties considered in this analysis. For each uncertainty, the number of used variations is provided together with a short description. In total, 88 uncertainties were considered by applying 350 variations.

A.2. Samples

Category	DSID	Event generation tag	simulation tag	reconstruction tags	production tag
tZq	512059	e8400	a907	r14859, r14860, r14861	p6266
ttZ	504330 504334 504342	e8255	s3797	r13167, r13144, r13145	p6266
tWZ	410408	e6423	s3681	r13167, r13144, r13145	p5855
Diboson	364250 364253 364284 364288	e5894 e5916 e6055 e6096	s3681	r13167, r13144, r13145	p6266
	345705 345706	e6213			
ttX	700706	e8470	a907	r14859, r14860, r14861	p6266
	410389	e6155	s3681	r13167, r13144, r13145	p5855
	346343 346344 346345	e7148			p6284
	504338 504346	e8255	s3797		6266

Fakes	364100	e5271	s3681	r13167, r13144, r13145	p6026
	364101				
	364102				
	364103				
	364104				
	364105				
	364106				
	364107				
	364108				
	364109				
	364110				
	364111				
	364112				
	364113				
	364114	e5299			
	364115				
	364116				
	364117				
	364118				
	364119				
	364120				
	364121				
	364122				
	364123				
	364124				
	364125				
	364126				
	364127				
	364128	e5307			
	364129				
	364130				
	364131				
	364132				
	364133				
	364134				
	364135				
	364136				
	364137				
	364138				
	364139				
	364140				
	364141				
	410472	e6348			p6266

Vyjets_ll	700398	e8338	s3681	r13167, r13144, r13145	p6266
	700399				
	700400				
	700401				
	700402				
	700403				
	700404				
Other	304014	e4324	s3681	r13167, r13144, r13145	p6266
	363358	e5525			
	363359	e5583			
	363360	e5983			
	364242	e5887			
	364243				
	364244				
	364245				
	364246				
	364247				
	364248				
	364249				
	410081	e4111			
	346310	e7151			
	346311				
	346312				
	412043	e7101	a907	r14859, r14860, r14861	p5855
SMEFT-tZq	508772	e8379	a907	r14859, r14860, r14861	p6160
	508773				p6214
SMEFT-ttZ	508985	e8379	a907	r14859, r14860, r14861	p6214
	508986				
SMEFT-tWZ	510212	e8470	a907	r14859, r14860, r14861	p6214
	510213				

Table A.2.: List of all MC generated samples used in the analysis. Samples are sorted by the processes described. The different tags associated to the simulation and production steps are listed as well.

A.3. Additional plots from EFT fits

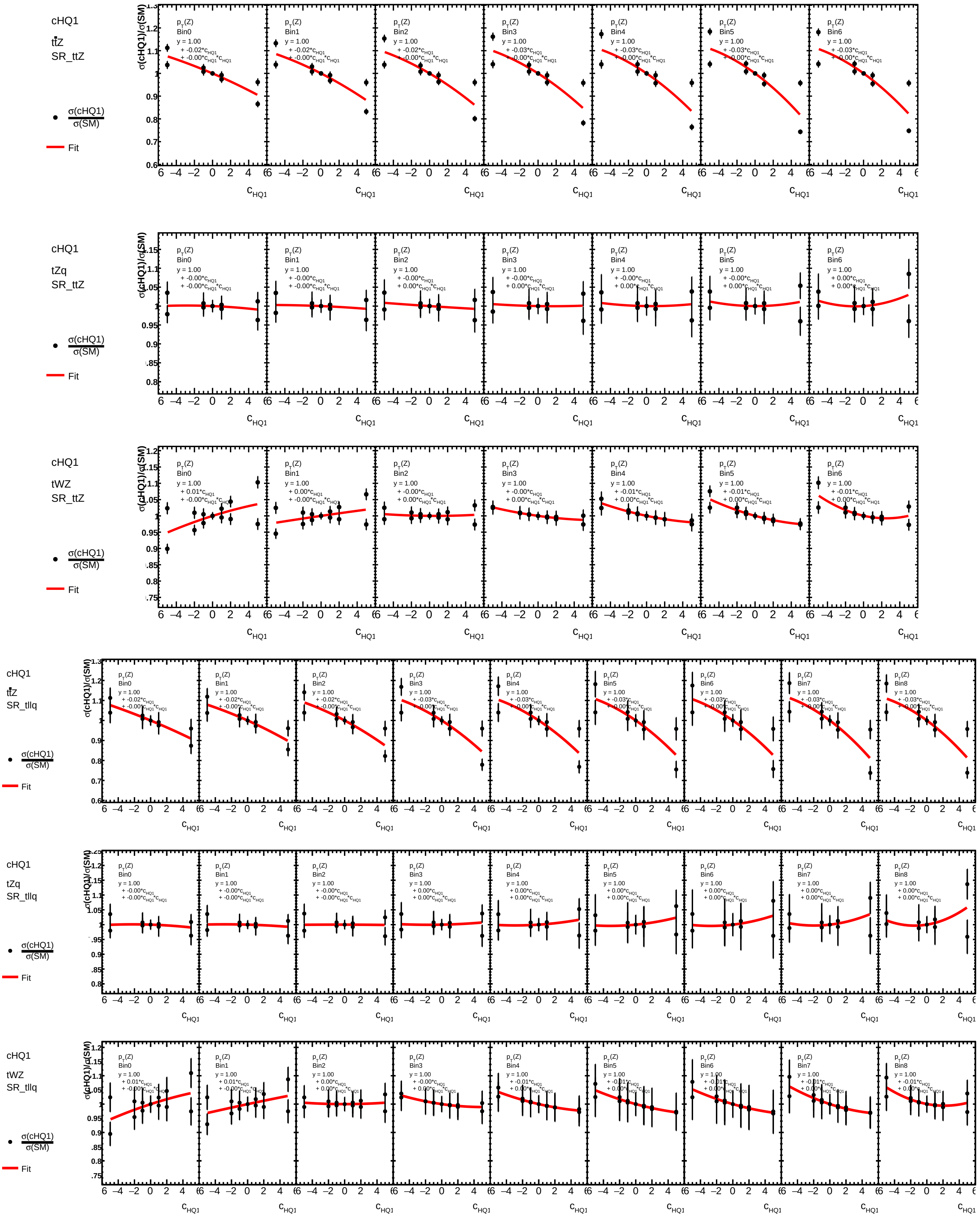

Figure A.1.: Results of the quadratic fit performed in each bin to parametrize the effect of the Wilson coefficient $c_{HQ}^{(1)}$.

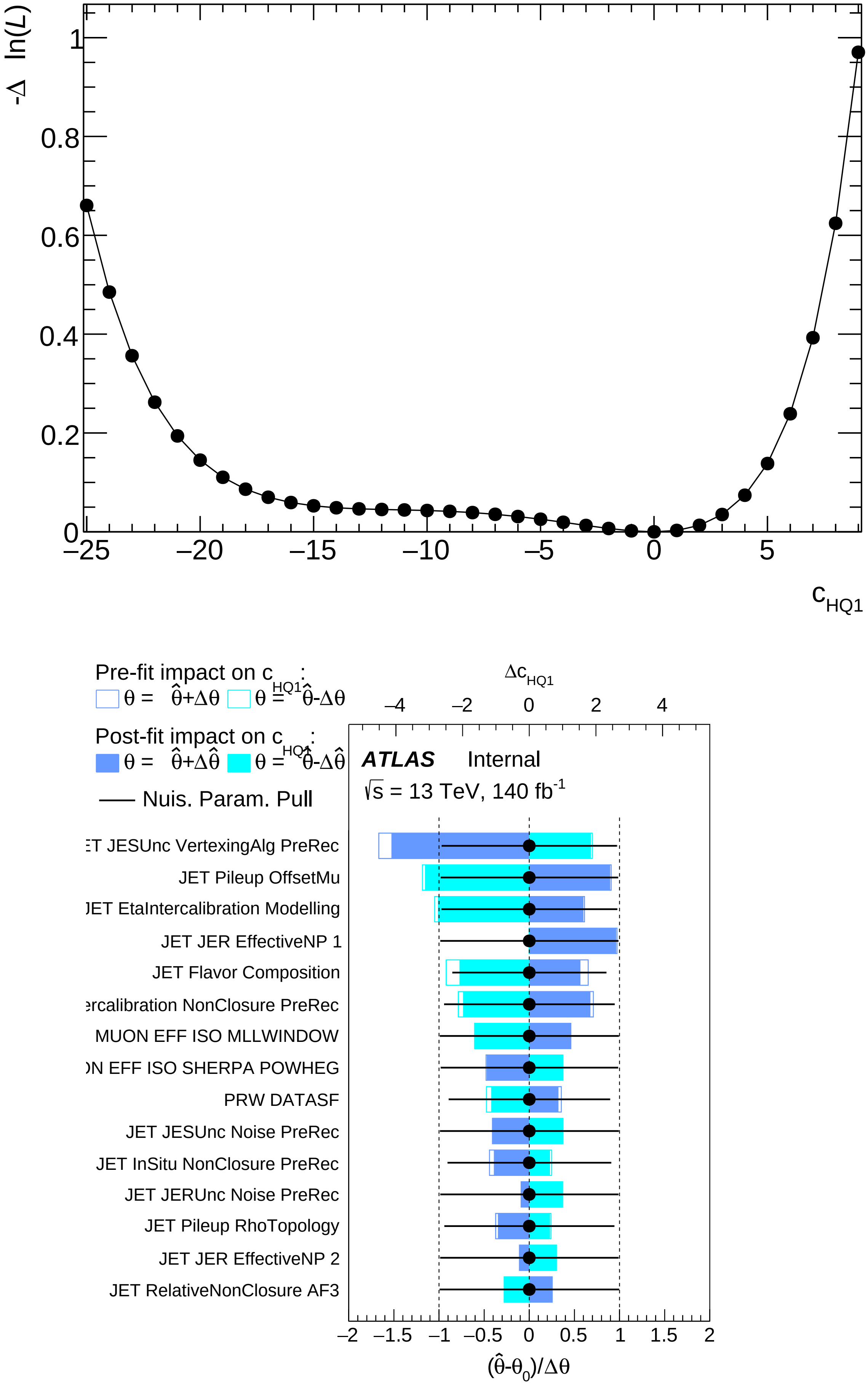

Figure A.2.: Likelihood scan for different values of the Wilson coefficient $c_{HQ}^{(1)}$ (top) and ranking of the 15 leading nuisance parameters (bottom).

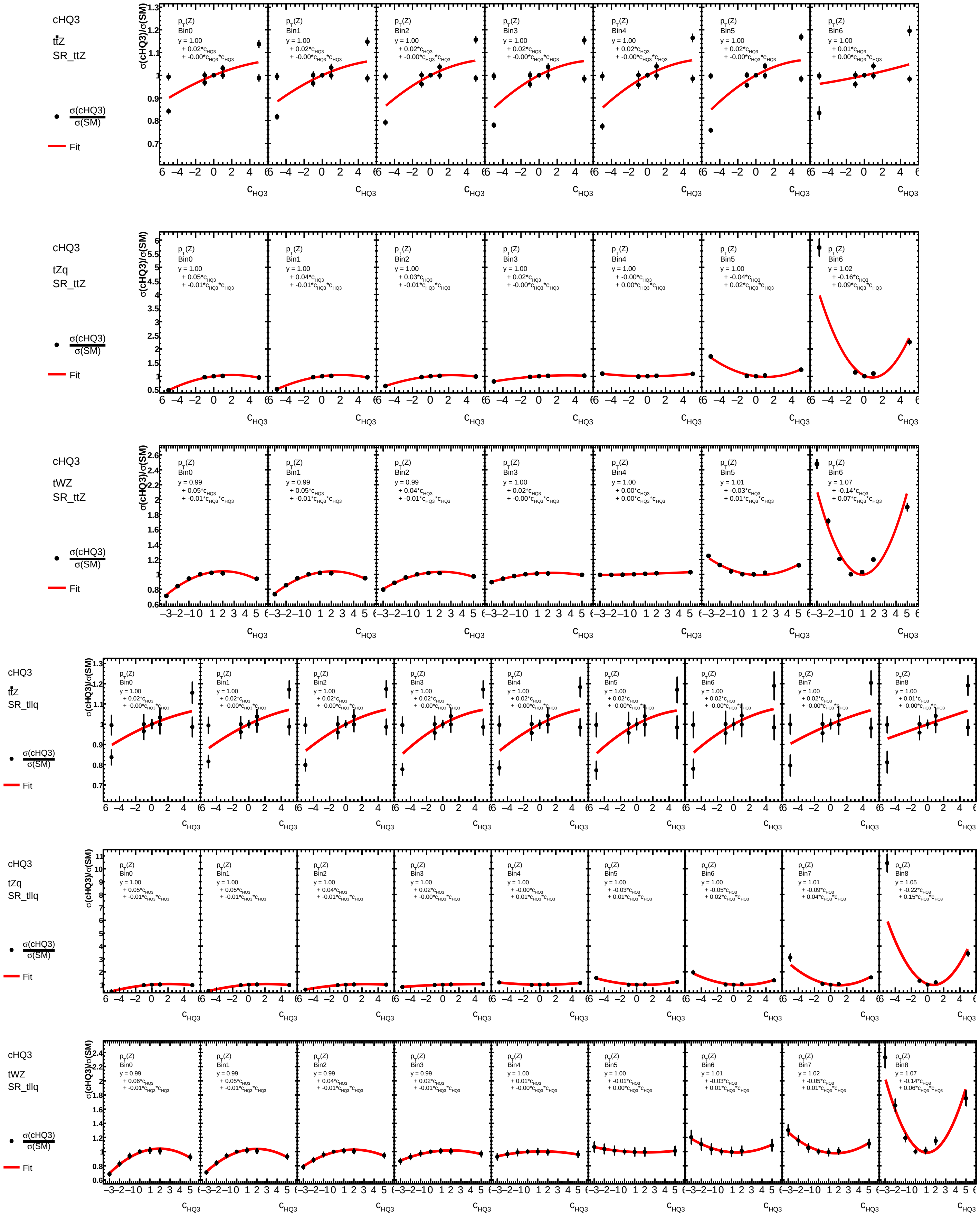

Figure A.3.: Results of the quadratic fit performed in each bin to parametrize the effect of the Wilson coefficient $c_{HQ}^{(3)}$.

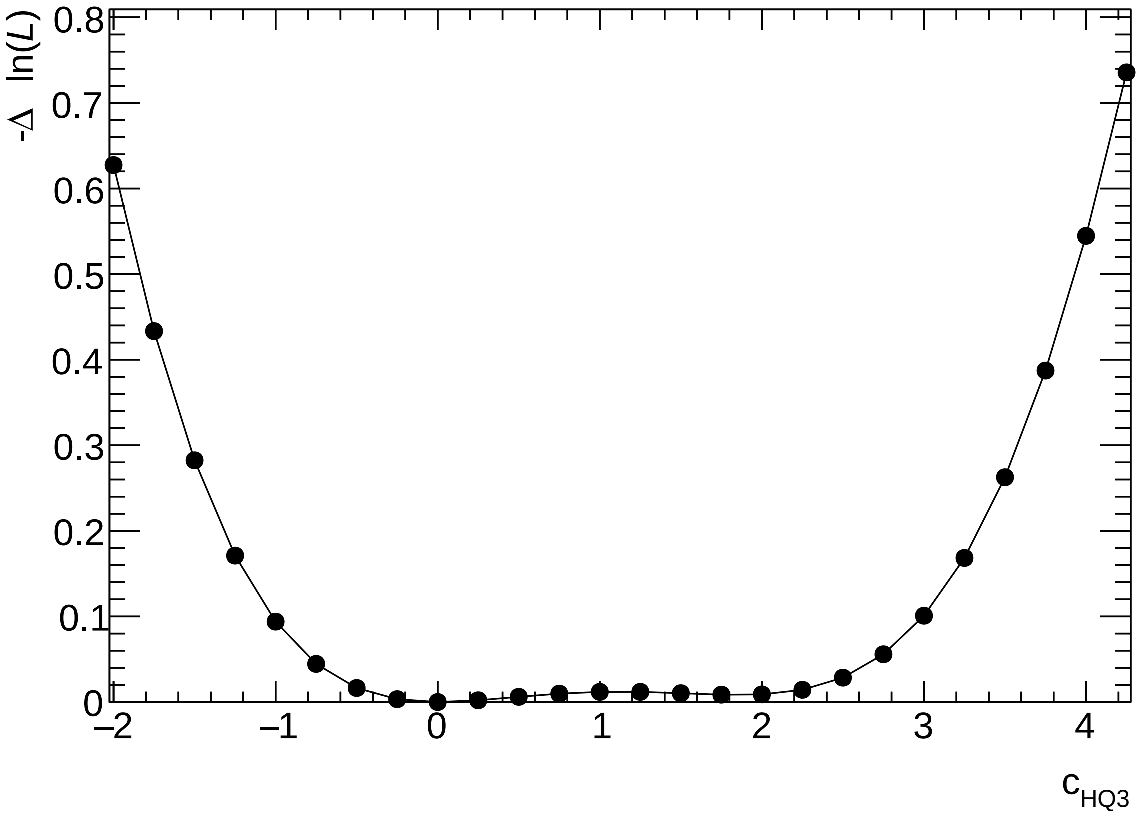

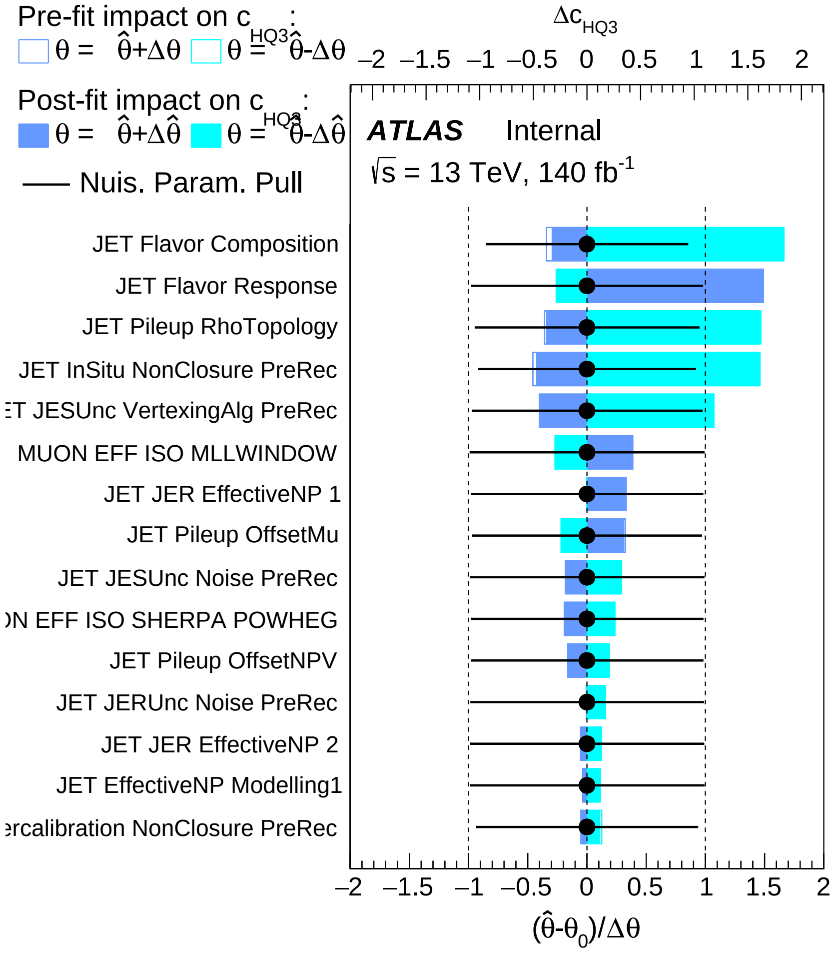

Figure A.4.: Likelihood scan for different values of the Wilson coefficient $c_{HQ}^{(3)}$ (top) and ranking of the 15 leading nuisance parameters (bottom).

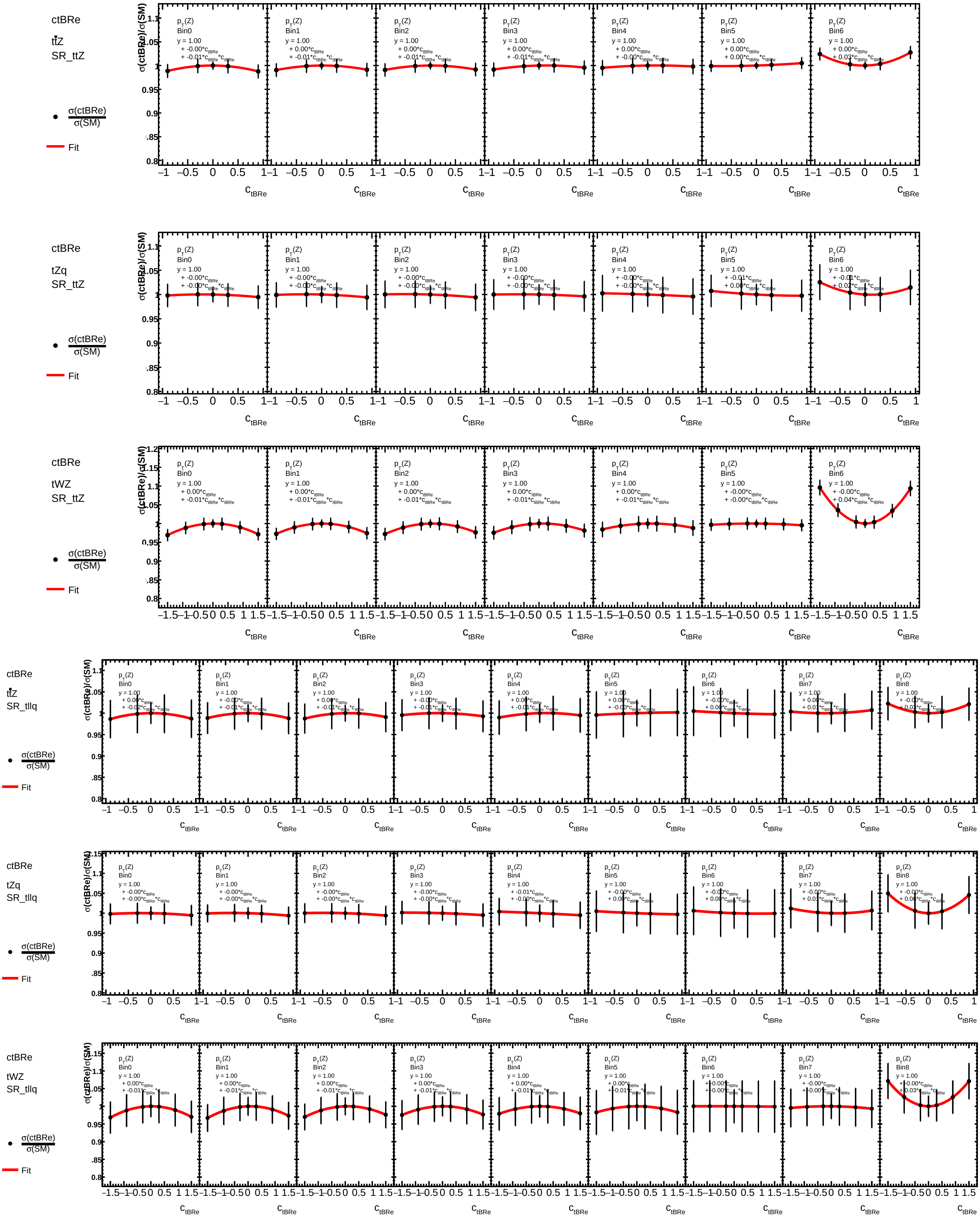

Figure A.5.: Results of the quadratic fit performed in each bin to parametrize the effect of the Wilson coefficient $c_{tB}^{(\mathrm{Re})}$.

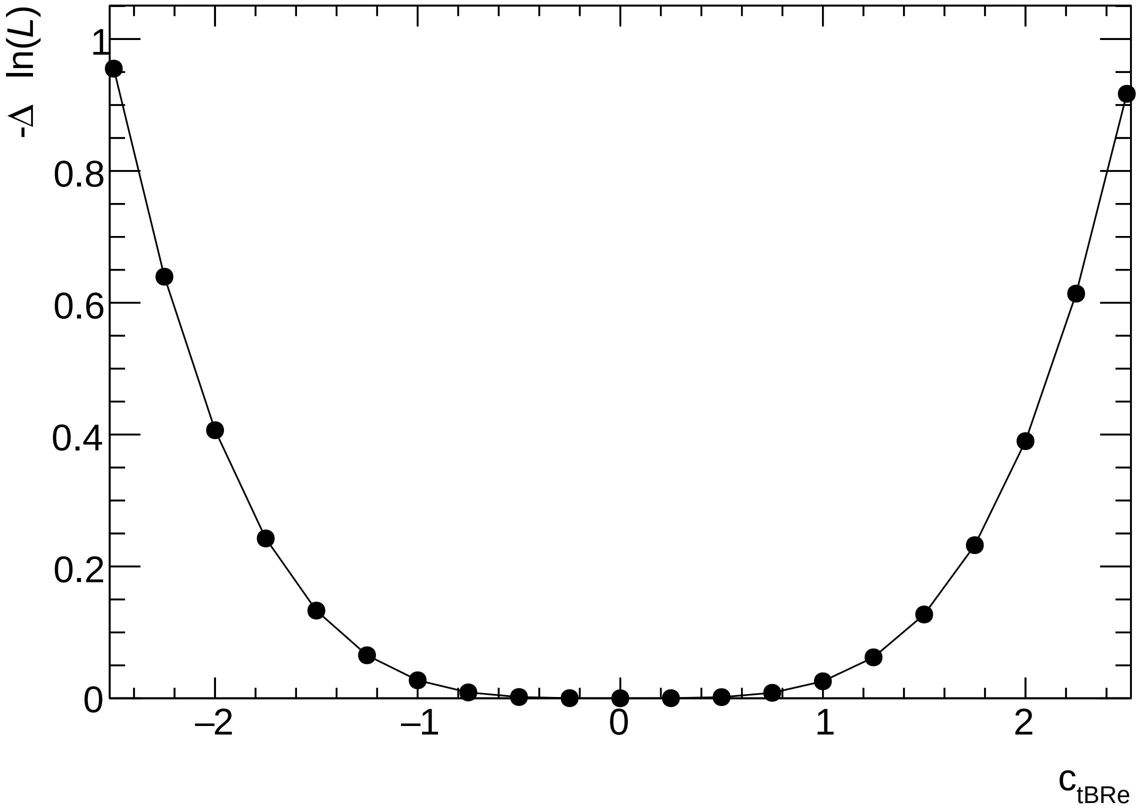

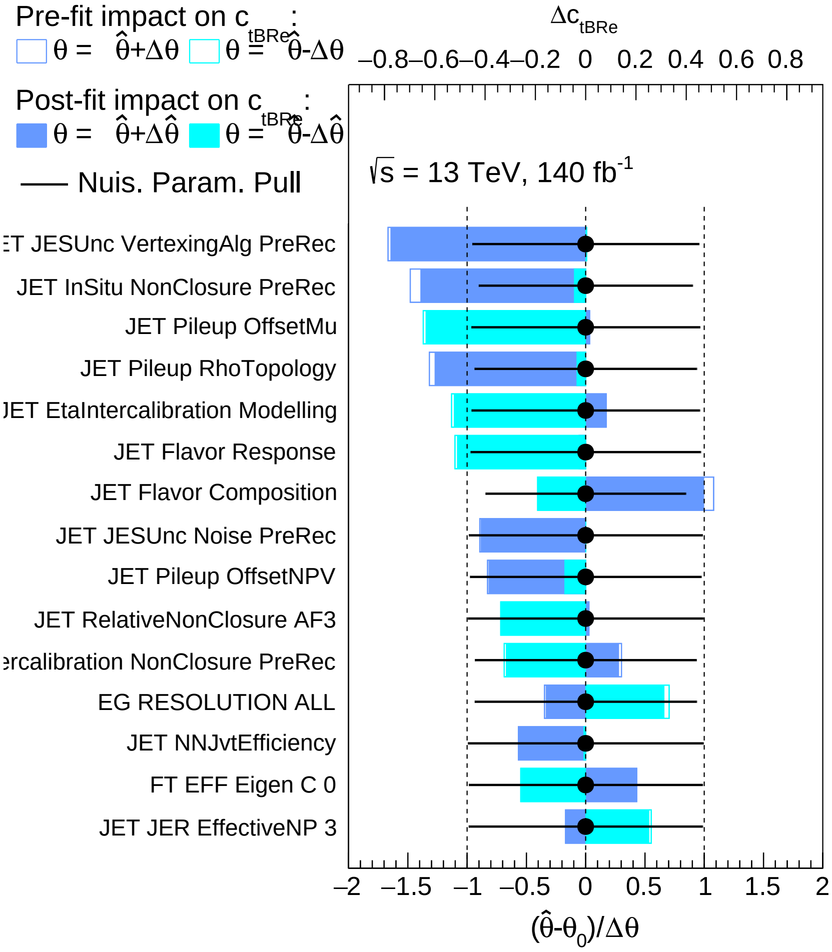

Figure A.6.: Likelihood scan for different values of the Wilson coefficient $c_{tB}^{(\mathrm{Re})}$ (top) and ranking of the 15 leading nuisance parameters (bottom).

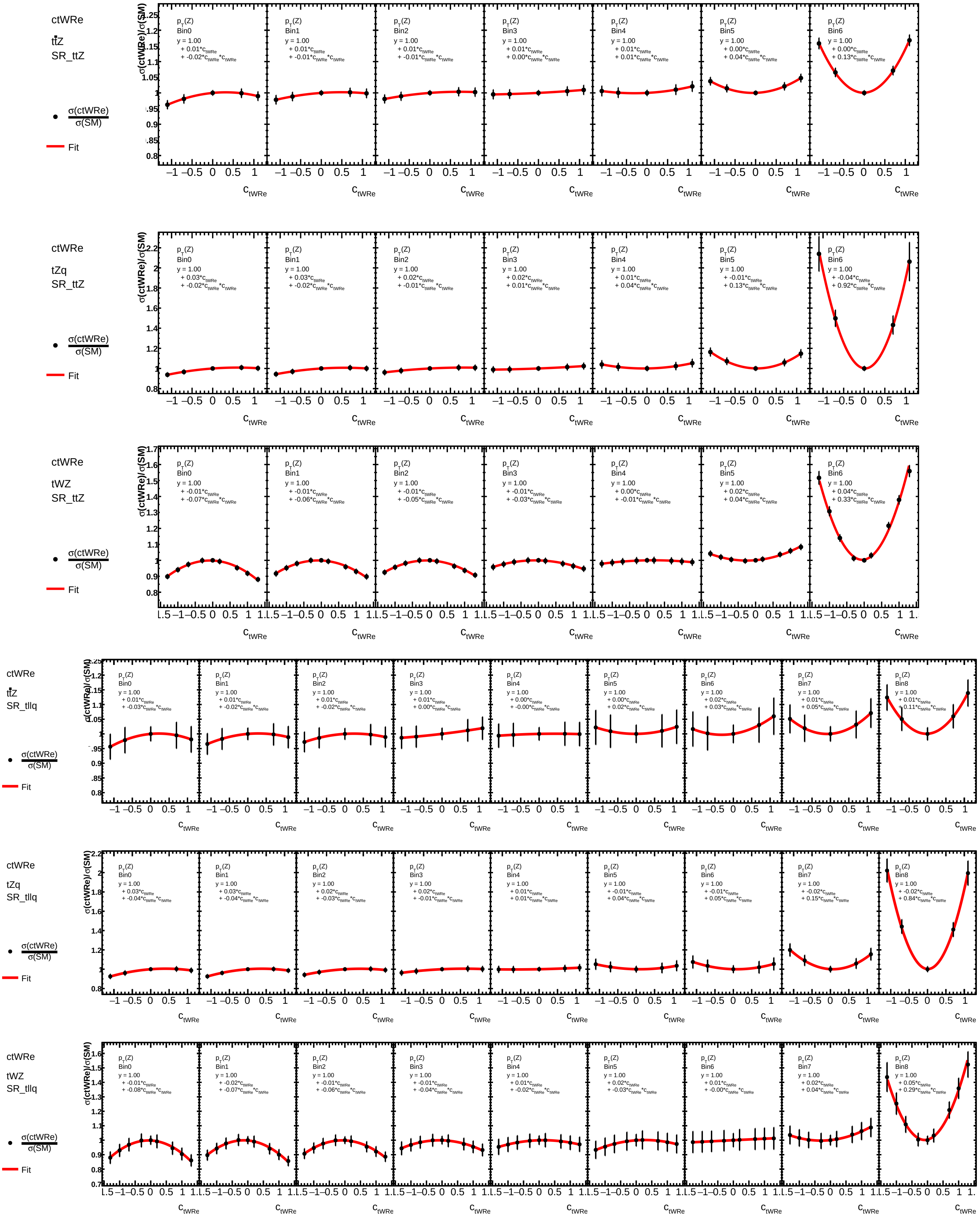

Figure A.7.: Results of the quadratic fit performed in each bin to parametrize the effect of the Wilson coefficient $c_{tW}^{(\mathrm{Re})}$.

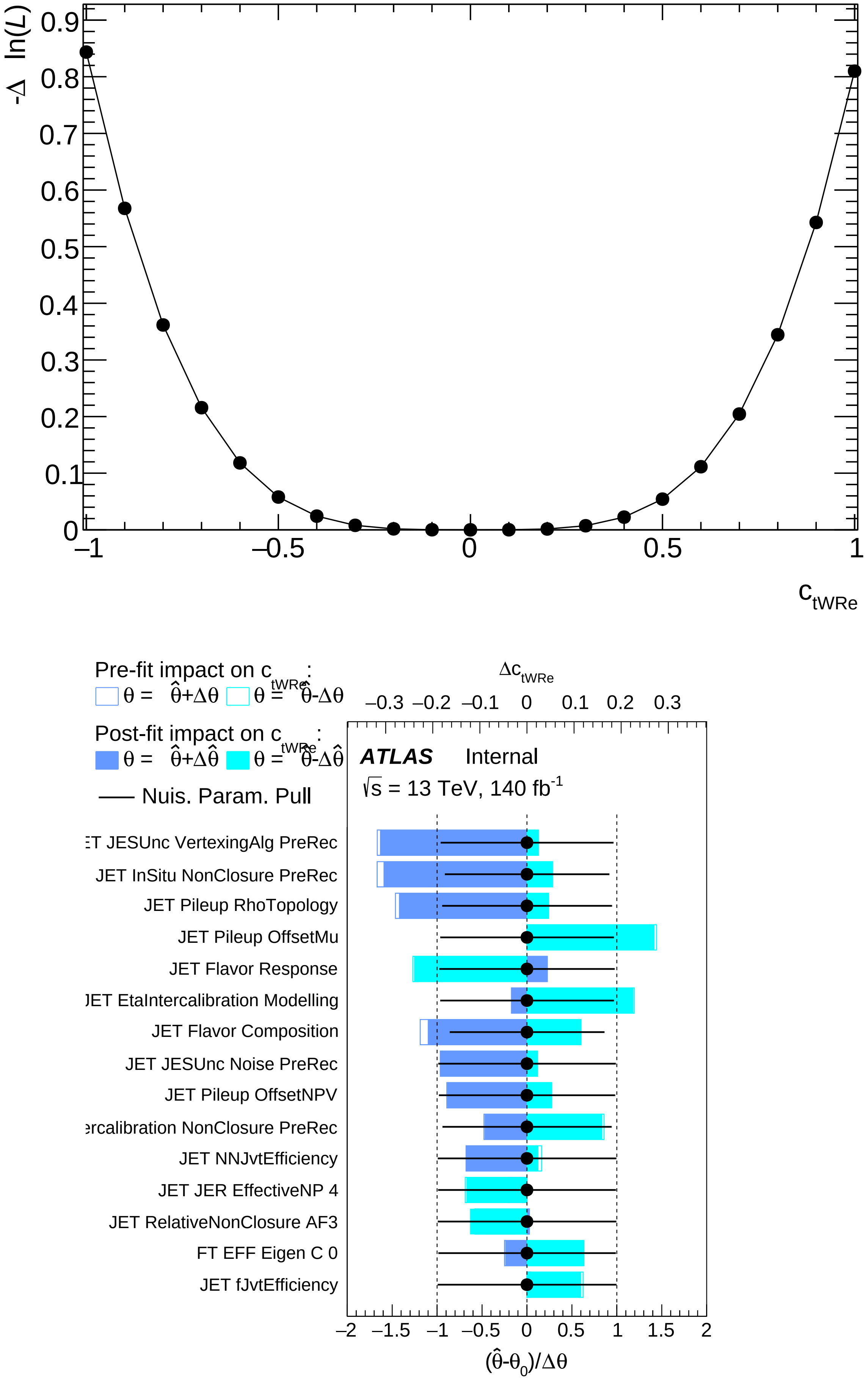

Figure A.8.: Likelihood scan for different values of the Wilson coefficient $c_{tW}^{(\mathrm{Re})}$ (top) and ranking of the 15 leading nuisance parameters (bottom).

Acknowledgements

I would like to thank Prof. Arnulf Quadt for the opportunity to write my master's thesis in his group and with his supervision and be part of the ATLAS collaboration. My time in the group taught me a lot about physics, data analysis, and the work in a research group. I would also like to thank Dr. Baptiste Ravina for his close supervision and regular input as an expert on the physics background of EFT searches. Working with the new tools you co-developed taught me a lot about programming and data analysis at ATLAS now and in the years to come. This thesis would not be the same without the support of Dr. Steffen Korn, who was always available and willing to help with any questions surrounding my work. Your experience with $t\bar{t}Z$ analyses often helped me understand the problems I encountered and the results I obtained. I owe Steffen and Baptiste a lot of gratitude for proofreading this thesis.
Lastly, I want to express my appreciation for all members of the II. Institute of Physics, with whom I spend many lunch breaks and after-work get-togethers. You made for a welcoming environment throughout the last years and provided moral support through the stressful times that are part of every thesis.

Erklärung nach §17(9) der Prüfungsordnung für den Bachelor-Studiengang Physik und den Master-Studiengang Physik an der Universität Göttingen: Hiermit erkläre ich, dass ich diese Abschlussarbeit selbständig verfasst habe, keine anderen als die angegebenen Quellen und Hilfsmittel benutzt habe und alle Stellen, die wörtlich oder sinngemäß aus veröffentlichten Schriften entnommen wurden, als solche kenntlich gemacht habe.

Darüberhinaus erkläre ich, dass diese Abschlussarbeit nicht, auch nicht auszugsweise, im Rahmen einer nichtbestandenen Prüfung an dieser oder einer anderen Hochschule eingereicht wurde.

Göttingen, den 30. September 2024

(Daniel Werner)